

Generating microstructures of long fiber reinforced composites by the fused sequential addition and migration method

Celine Lauff¹  | Matti Schneider²  | John Montesano³ | Thomas Böhlke¹ 

¹Institute of Engineering Mechanics, Karlsruhe Institute of Technology (KIT), Karlsruhe, Germany

²Institute of Engineering Mathematics, University of Duisburg-Essen, Essen, Germany

³Department of Mechanical and Mechatronics Engineering, University of Waterloo, Waterloo, Canada

Correspondence

Thomas Böhlke, Institute of Engineering Mechanics, Karlsruhe Institute of Technology (KIT), Karlsruhe, Germany.
Email: thomas.boehlke@kit.edu

Abstract

We introduce the fused sequential addition and migration (fSAM) algorithm for generating microstructures of fiber composites with long, flexible, nonoverlapping fibers and industrial volume fractions. The proposed algorithm is based on modeling the fibers as polygonal chains and enforcing, on the one hand, the nonoverlapping constraints by an optimization framework. The connectivity constraints, on the other hand, are treated via constrained mechanical systems of d'Alembert type. In case of straight, that is, nonflexible, fibers, the proposed algorithm reduces to the SAM (*Comput. Mech.*, 59, 247–263, 2017) algorithm, a well-established method for generating short fiber-reinforced composites. We provide a detailed discussion of the equations governing the motion of a flexible fiber and discuss the efficient numerical treatment. We elaborate on the integration into an existing SAM code and explain the selection of the numerical parameters. To capture the fiber length distributions of long fiber reinforced composites, we sample the fiber lengths from the Gamma distribution and introduce a strategy to incorporate extremely long fibers. We study the microstructure generation capabilities of the proposed algorithm. The computational examples demonstrate the superiority of the novel microstructure-generation technology over the state of the art, realizing large fiber aspect ratios (up to 2800) and high fiber volume fractions (up to 32% for an aspect ratio of 150) for experimentally measured fiber orientation tensors.

KEYWORDS

curved fibers, d'Alembert type constrained mechanical systems, fused sequential addition and migration, long fiber reinforced composites, microstructure generation, representative volume elements

1 | INTRODUCTION

1.1 | State of the art

Long fiber reinforced thermoplastics (LFT) offer a high potential for lightweight applications as they feature a high stiffness to weight ratio and may be manufactured with cost-efficient processes as injection or compression molding. Due to

This is an open access article under the terms of the [Creative Commons Attribution-NonCommercial-NoDerivs](https://creativecommons.org/licenses/by-nc-nd/4.0/) License, which permits use and distribution in any medium, provided the original work is properly cited, the use is non-commercial and no modifications or adaptations are made.

© 2024 The Author(s). *International Journal for Numerical Methods in Engineering* published by John Wiley & Sons Ltd.

the heterogeneity of these composites, their elastic and inelastic mechanical behavior depends strongly on the material microstructure and the properties of the constituents. Hence, understanding the underlying microstructures is essential for predicting the effective properties of LFT properly. Characterizing such composites with micro-CT imaging^{1–4} reveals highly anisotropic and random geometries, mainly described by the fiber volume fraction, the fiber length and orientation distributions, as well as the fiber curvature.

To predict the mechanical behavior of such heterogeneous materials, multiscale methods,⁵ in particular using advanced computational approaches,^{6–8} offer a time and resource efficient alternative compared to an experiments-only approach. However, computational strategies require a complete description of the considered microstructure to be provided.⁹ Moreover, for random materials combining periodic geometries with periodic boundary conditions (required for the homogenization) is particularly advantageous for computational multiscale methods.^{10–12}

Typically, images of LFT from micro-CT scanning^{1–4} are available and may be used to obtain the necessary digital microstructures. However, extracting a complete geometrical description from these images suffers from inaccuracies, for example, as a result of the limited resolution with respect to the segmentation of the fibers. Additionally, the resulting geometries are nonperiodic and subsequent periodization¹¹ is a demanding task. As a further restriction, only digital microstructures corresponding to the available micro-CT images are obtained. Due to the limited amount of data, investigating the mechanical behavior for more general cases is impossible. In this context, microstructure generation algorithms are used to obtain periodic microstructures for prescribed microstructure characteristics, for example, the fiber volume fraction or the fiber length and orientation distributions.

In general, methods for generating particle composites may be roughly classified into two categories: sequential insertion algorithms and collective rearrangement algorithms. For sequential insertion algorithms, the particles are placed one by one, keeping the positions and orientations of the previously placed inclusions fixed. The prime representative of this class is the random sequential addition (RSA) algorithm initially introduced for spheres¹³ and subsequently extended to more general inclusion shapes.¹⁴ Until the desired fiber volume fraction is reached, particles are placed successively under the condition of mutual nonintersection. More precisely, for each fiber, its direction, length and midpoint are sampled randomly from suitable distribution functions until an admissible, that is, nonoverlapping, configuration is found. In case a generated fiber is not placed in a nonoverlapping position, there are two typical strategies for re-sampling. Either only the midpoint is sampled anew or the direction and length as well. The latter strategy permits to reach higher fiber volume fractions than the former. This increase, however, comes at a cost—systematic deviations of the desired orientation and length distribution functions may be unavoidable then.

For sequential insertion algorithms, the particle characteristics are permanent after its placement, that is, it will never be moved thereafter. Hence, the achievable fiber volume fraction is comparatively low. Moreover, with increasing fiber aspect ratio r_a , that is, the ratio between fiber length and diameter, the achievable fiber volume fraction decreases as well.^{15,16} In fact, RSA-type methods permit to realize high volume fraction for unidirectional fiber arrangement only. Nevertheless, the RSA algorithm is the most common microstructure generator and a number of extensions are available.^{17–22}

The second category of microstructure-generation algorithms for matrix-inclusion composites comprises methods which position all particles in the cell first and then change their positions simultaneously. The mechanical contraction method (MCM) introduced by Williams and Philipse²³ permits to generate microstructures of spherocylinders, that is, cylinders with half-caps at their ends, are generated. In the first step of the MCM, RSA is used to generate a microstructure with small volume fraction and nonoverlapping fiber configuration. Then, the unit cell is shrunk while retaining the size of the inclusions to increase the volume fraction. The resulting fiber overlap is removed by an iterative procedure. In its original form, the MCM is restricted to isotropic orientation states and fails to generate microstructures with industrial fiber volume fractions for long fibers. For more general fiber orientation distributions, the sequential addition and migration (SAM) algorithm may be used, first presented for short straight fibers with uniform length.²⁴ As starting point, a fiber arrangement is sampled according the descriptive components, for example, the fiber volume fraction or the fiber orientation distribution. In contrast to the MCM, in the starting configuration overlap between the fibers is allowed. Then, an optimization framework is used to find a configuration which satisfies the nonoverlap condition and further desired criteria. Therefore, a non-negative objective function is introduced where every configuration corresponding to a root of the objective function is admissible. Besides the SAM algorithm for short straight fibers with constant lengths,²⁴ also an extension for short fibers with fiber length distributions²⁵ is available. Using this extension, the SAM algorithm accounts for variability in the fiber lengths, which is typical for industrial discontinuous fiber-reinforced composites. Additionally, considering fiber length distributions instead of uniform fiber lengths increases the volume-weighted mean fiber length which can be realized by the algorithm. Thus, the SAM algorithm which accounts for a fiber length distribution

is capable of generating long fiber reinforced composites as PPGF30 (13.22% fiber volume fraction), when restricting the volume-weighted mean fiber length to about 2–3 mm. However, there are two apparent shortcomings of the original SAM algorithm. For a start, the generated unit cells can become quite large. In fact, due to the straight fibers, the side length of the unit cells need to be as long as the imposed mean fiber length, at least. This constraint may be rather restrictive for long fibers. Secondly, the straight-fiber model of the original SAM algorithm leads automatically to the formation of bundles of more or less aligned straight fibers. As such bundles of straight fibers are seldomly found in real composites, the effective properties of the composite may be overestimated by computations based on such unit cells.

To enable microstructure generation for industrial LFTs, the packing limit with increasing fiber aspect ratio needs to be overcome. However, to deal with this challenge, the reason for the packing limit should be understood first. In terms of general packing mechanics of straight fibers, Toll¹⁶ reveals that the fiber volume fraction may be increased until a maximum number of contacts per fiber is reached. By modeling the fibers with straight cylinders, this maximum number of contacts turns out to be independent of the fiber aspect ratio r_a . However, the apparent number of contacts during the microstructure generation is higher for increasing fiber aspect ratios. Hence, besides unidirectional fiber arrangement less fiber volume fraction is achieved for increasing fiber aspect ratios. With this insight at hand, we conclude that modeling the fibers with straight cylinders restricts the achievable fiber volume fraction due to their low maximum number of contacts. To overcome this limitation, modeling fibers accounting for fiber bending may enable packings with higher volume fractions for longer fibers.¹⁶ Moreover, this appears to be the more natural way of describing real fibers in long fiber reinforced composites as they feature significant fiber bending due to the manufacturing processes.

For typical manufacturing processes, long fiber reinforced composites feature almost planar fiber orientation states^{26–29} as the fiber lengths exceed the plate thickness. For these cases, Fliegner et al.³⁰ present an algorithm for microstructure generation with curved fibers achieving high fiber volume fractions. First, a planar microstructure with low fiber volume fraction is generated by RSA. Then, the structure is compressed in thickness direction using a full finite element analysis until the required volume fraction is reached. Due to the finite element analysis, the method is computationally complex and time-consuming, as many elements are necessary to resolve the microstructure adequately. Additionally, changing the resolution after the microstructure generation, for example, for the homogenization, is a challenging topic as the fibers are modeled with hexahedral elements and not with an underlying analytical formulation.

An alternative approach accounting for fiber bending, is the extension of the SAM algorithm for long curved fibers.³¹ For this algorithm, a curved fiber is discretized by a polygonal chain with spherocylinders as segments. Thus, the optimization problem incorporates the additional condition that adjacent segments need to be connected. In general, such a constraint may be considered in the optimization process in two ways. On one hand, the constraint may only be satisfied at convergence and may be violated for previous iterative steps. For the previous SAM approach, this is realized by adding a penalty term to the objective function. To make this strategy work, the penalty parameter needs to be selected in a clever way and may influence the convergence behavior negatively. The alternative strategy satisfies the constraint in every step, resulting in a more complex iteration rule. Within the optimization procedure of the SAM algorithm for long curved fibers,³¹ the first strategy is used. Hence, the segments move separately during the optimization process. However, the penalty term leads to convergence problems for complex microstructures. Thus, microstructures with high fiber volume fractions are barely achieved.

1.2 | Contributions

In this work, we address the challenge of generating packings with high fiber volume fractions for long fiber-reinforced composites. More precisely, we aim to realize microstructures for industrial composites with fiber volume fractions up to 30% and aspect ratios exceeding 100. For the microstructure generation, we address two further tasks. First, the size of the representative volume element (RVE) needs to be reduced to enable efficient microstructure generation and computational homogenization. Therefore, we require the descriptive components of the microstructure to be realized accurately. Additionally, we wish to generate periodic geometries to decrease artificial artifacts at the boundaries.^{10–12} Moreover, we aim to account for the fiber bending, as modeling fibers with straight cylinders necessitates RVEs to be rather large.^{32,33} Secondly, we target an adequate modeling of the fiber lengths. Experiments reveal that long fiber reinforced composites feature fiber length distributions with high standard deviations^{30,34,35} leading to a wide range of fiber lengths. Computing the effective properties requires that the fiber length distribution is captured accurately, that is, assuming constant fiber lengths is not sufficient.²⁵ Thus, we require an adequate representation of the fiber length distribution.

To address these tasks, we present the fused Sequential Addition and Migration (fSAM) algorithm as an alternative approach to the SAM strategy for long curved fibers³¹ in terms of a physically meaningful fiber motion during the optimization. The SAM strategy for long curved fibers discretizes the curved fibers as polygonal chains. Hence, besides other criteria for convergence, for example, the nonoverlap condition, adjacent segments need to be connected. A *converged* configuration satisfying the nonoverlap condition and the coherence condition for all fibers is shown in Figure 1. During the optimization procedure with a gradient descent approach, Schneider³¹ moves the segments of each polygonal chain independently. To ensure the coherence condition between adjacent segments, a penalty term is added to the optimization function. As the coherence condition is not fulfilled for all iterative steps, nonconverged configurations typically show a positive distance between the fiber segments. A nonconverged configuration of the SAM algorithm is shown in Figure 1, where we highlight the distance between adjacent segments by the dashed connection lines. Due to the additional penalty term, the SAM strategy for long curved fibers suffers from convergence problems for complex microstructures. To overcome this limitation, we aim to fulfill the coherence condition in every iterative step by moving the polygonal chains in a fused way. Hence, nonconverged configurations of the fSAM algorithm involve connected fibers, see Figure 1. However, by restricting the movement on the admissible space for a connected polygonal chain, the configuration space, that is, the admissible set during the optimization, is a curved, that is, nonflat, manifold. In this context, a basic gradient descent approach may lead to iterates which leave the manifold. We illustrate this issue for an optimization problem where the configuration space for the iterates $\mathbf{p}^k \in \mathbb{R}^2$ is the unit circle, see Figure 2A. For Riemannian manifolds (\mathcal{M}, g) with metric g , an optimization on the manifold may be ensured by moving along the geodesics,^{36,37} that is, the shortest lines between two points on the manifold. These replace the straight lines in vector spaces, where no curvature is present. In Figure 2B, a gradient descent step following the geodesic of the unit sphere is shown. In general, the equations governing the geodesics may be understood as mechanical problems with holonomic constraints and no external forces. Hence, moving along a geodesic means integrating the constrained mechanical system for a unit time with initial conditions, that is, the location on the manifold and a tangent vector. For enabling fused fiber

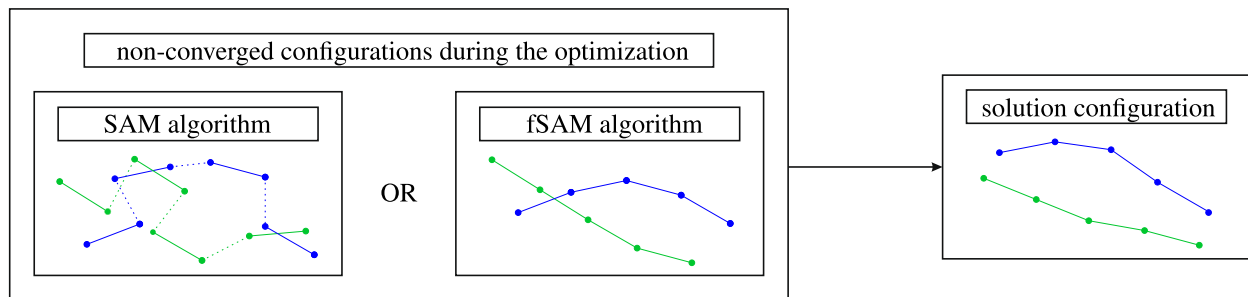


FIGURE 1 Visualization of nonconverged configurations during the optimization using the SAM algorithm or the fSAM algorithm as well as of a solution configuration.

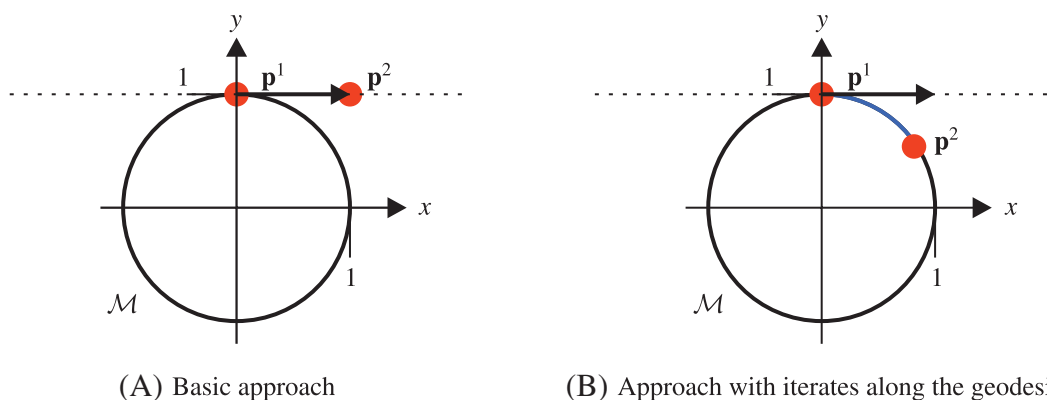


FIGURE 2 Illustration of a gradient descent step with the iterates \mathbf{p}^1 and \mathbf{p}^2 for an optimization problem with a unit circle as the configuration space \mathcal{M} , using the basic approach (A) and an adapted approach moving along the blue highlighted geodesic (B).

movement, we first derive the d'Alembert type constrained mechanical system, which governs the geodesics of the manifold describing a polygonal chain. Then, we introduce an efficient numerical integration for the resulting differential algebraic equations.

We account for the fiber length distribution by sampling the fiber lengths from the Gamma distribution. The details comprise Section 3.3. As a result, extremely long fibers may occur, discretized with a high number of segments. However, the dimension of the system of equations which is solved for the numerical integration of the constrained mechanical system increases with the number of segments. As the effort of direct solvers scales cubically with the dimension, extremely long fibers lead to a rather long runtime. To handle this issue, we propose a workaround for extremely long fibers. To be more precise, a fiber discretized with more segments than a maximum number is divided in smaller subchains, which move separately. The coherence conditions between these subchains is only ensured for the final configuration by adding a respective penalty term to the optimization function. We refer to Section 3.4 for more details.

For the computational investigations described in Section 4, we first discuss the improvements of the microstructure generation with the fSAM algorithm by comparing it to the SAM algorithm for long fibers.³¹ After identifying the necessary resolution and RVE size, we study the influence of the maximum segment length which is used to discretize the curved fibers. Moreover, we show the capability of the fSAM algorithm to generate packings with high fiber volume fractions for long fibers. Furthermore, we apply the fSAM algorithm to an industrial PPGF30 material, comprised of a polypropylene matrix reinforced by E-glass fibers with a volume content of 13.22%, accounting for its fiber length distribution.

1.3 | Notation

Throughout this manuscript, a direct tensor notation or a matrix-vector-notation with orthonormal bases $\{\mathbf{e}_1, \dots, \mathbf{e}_n\}$ ($n \in \mathbb{N}$) is used. We denote scalars by nonbold letters, for example, b . Noncursive bold lowercase letters, for example, \mathbf{b} , are used for vectors in matrix-vector notation and cursive bold lowercase letters, for example, \mathbf{b} , for vectors in direct tensor notation. Matrices are denoted with bold noncursive uppercase letters, for example, \mathbf{B} . Tensors of second order are represented by bold cursive uppercase letters, for example, \mathbf{B} , and tensors of fourth order by, for example, \mathbb{B} . With respect to a three-dimensional vector space, a tensor of second order in diagonalized form is given with, for example, $\mathbf{B} \hat{=} \text{diag}(b_1, b_2, b_3)$. The following notation for the mathematical operations may be used for the direct tensor notation as well as for the matrix-vector notation. A transposed tensor of second order is given with, for example, \mathbf{B}^T . We denote a linear mapping of a first-order by a second-order tensor as, for example, $\mathbf{a} = \mathbf{C}\mathbf{b}$ and the linear mapping with complete contraction including higher-order tensors as, for example, $\mathbf{a} = \mathbb{B}[\mathbf{C}_{(3)}] \hat{=} B_{ijkl}C_{jkl}$. For the scalar product, we use the notation $\mathbf{A} \cdot \mathbf{B} = \text{tr}(\mathbf{A}\mathbf{B}^T)$ and for the Frobenius norm $\|\mathbf{B}\| = (\mathbf{B} \cdot \mathbf{B})^{1/2}$. The dyadic product is given with, for example, $\mathbf{a} \otimes \mathbf{b}$ and the l -times repeated dyadic product of a vector with, for example, $\mathbf{b}^{\otimes l} = \mathbf{b} \otimes \mathbf{b} \cdots \otimes \mathbf{b}$. We represent the unit sphere in \mathbb{R}^3 by S^2 . For the cross product of two vectors, we use the notation, for example, $\mathbf{a} \times \mathbf{b}$. A skew-symmetric tensor of second order with corresponding axial vector \mathbf{b} is denoted by $\mathbf{b} \times \hat{=} (\mathbf{b} \times)_{ij} = \varepsilon_{ikj}b_k$, using the permutation symbol

$$\varepsilon_{ijk} = \begin{cases} +1, & \text{for } (i, j, k) = (1, 2, 3), (2, 3, 1), \text{ or } (3, 1, 2), \\ -1, & \text{for } (i, j, k) = (1, 3, 2), (2, 1, 3), \text{ or } (3, 2, 1), \\ 0, & \text{else.} \end{cases} \quad (1)$$

2 | OPTIMIZATION ON THE CONFIGURATION SPACE OF CURVED FIBERS

2.1 | Riemannian manifolds and submanifolds

In this article, we consider *Riemannian manifolds* (\mathcal{M}, g) ,^{36,37} that is, real, smooth manifolds \mathcal{M} equipped with a metric g , which is a family of Euclidean inner products on the tangent spaces $T_{\mathbf{x}}\mathcal{M}$ that depends smoothly on the point $\mathbf{x} \in \mathcal{M}$. With the metric, the energy of a curve $\mathbf{c} : [0, 1] \rightarrow \mathcal{M}$, parametrized by arc length t , is defined by

$$E(\mathbf{c}) = \frac{1}{2} \int_0^1 g_{\mathbf{c}(t)}^{\mathcal{M}}(\dot{\mathbf{c}}(t), \dot{\mathbf{c}}(t)) dt. \quad (2)$$

Suppose that a submanifold \mathcal{M} of the n -dimensional Euclidean space \mathbb{R}^n with scalar product $\langle \cdot, \cdot \rangle_{\mathbb{R}^n}$ is given in terms of a constraint function Φ which has $\mathbf{0}$ as a regular value. Then, the tangent space $T_{\mathbf{x}}\mathcal{M}$ arises as the null space of the constraint Jacobian

$$T_{\mathbf{x}}\mathcal{M} = \text{null}\left(\frac{\partial\Phi(\mathbf{x})}{\partial\mathbf{x}}\right), \quad \mathbf{x} \in \Phi^{-1}(\mathbf{0}) \equiv \mathcal{M}. \quad (3)$$

The submanifold \mathcal{M} naturally inherits the Riemannian metric of the ambient space

$$g_{\mathbf{x}}(\mathbf{v}_1, \mathbf{v}_2) = \langle \mathbf{v}_1, \mathbf{v}_2 \rangle_{\mathbb{R}^n}, \quad \mathbf{v}_1, \mathbf{v}_2 \in T_{\mathbf{x}}\mathcal{M} \subseteq \mathbb{R}^n. \quad (4)$$

For such a submanifold \mathcal{M} , the geodesic, that is, the shortest path between two points on the manifold,^{36,37} is obtained as the minimum of the energy functional in Equation (2)

$$\frac{1}{2} \int_0^1 g_{\mathbf{x}}(\dot{\mathbf{c}}(t), \dot{\mathbf{c}}(t)) dt \rightarrow \min_{\mathbf{c}: [0,1] \rightarrow \mathbb{R}^n, \text{ s.t. } \Phi(\mathbf{c}(t)) = \mathbf{0}} \quad (5)$$

subject to the constraints $\mathbf{c}(0) = \mathbf{x}_0$ and $\mathbf{c}(1) = \mathbf{x}_1$ for two given points $\mathbf{x}_0, \mathbf{x}_1 \in \mathcal{M}$. The optimization problem in Equation (5) may be interpreted as a constrained mechanical system following Newton's (generalized) laws of motion without a potential or external forces. Hence, the equations governing the geodesic motion on the manifold \mathcal{M} may be formulated in the form of the differential-algebraic equations (DAEs) for a general constrained mechanical system^{38,39}

$$\begin{aligned} \mathbf{M}\dot{\mathbf{c}}(t) + \mathbf{R}(\mathbf{c}(t), \lambda(t)) &= \mathbf{0} \quad \text{with} \quad \mathbf{R}(\mathbf{c}(t), \lambda(t)) \equiv \left(\frac{\partial\Phi(\mathbf{c}(t))}{\partial\mathbf{c}}\right)^T \lambda(t), \\ \Phi(\mathbf{c}(t)) &= \mathbf{0}, \end{aligned} \quad (6)$$

depending on a constant symmetric positive-definite (mass) matrix \mathbf{M} , a coordinate vector $\mathbf{c}(t)$, a vector the Lagrangian multipliers $\lambda(t)$ and a vector-valued constraint function Φ . The constraint forces are given with

$$\mathbf{R}(\mathbf{c}(t), \lambda(t)) \equiv \left(\frac{\partial\Phi(\mathbf{c}(t))}{\partial\mathbf{c}}\right)^T \lambda(t) \equiv \mathbf{J}(\mathbf{c}(t))^T \lambda(t), \quad (7)$$

where \mathbf{J} denotes the Jacobian of the vector-valued constraint function. Suppose that we parametrize a Riemannian manifold (\mathcal{M}, g) by another manifold \mathcal{M}_E with a smooth map

$$\mathbf{m} : \mathcal{M}_E \rightarrow \mathcal{M}. \quad (8)$$

Then, the manifold \mathcal{M}_E inherits the Riemannian metric g via pull-back³⁷

$$h_{\mathbf{p}}(\mathbf{w}_1, \mathbf{w}_2) \equiv g_{\mathbf{m}(\mathbf{p})}(d\mathbf{m}_{\mathbf{p}}(\mathbf{w}_1), d\mathbf{m}_{\mathbf{p}}(\mathbf{w}_2)), \quad \mathbf{p} \in \mathcal{M}_E, \quad \mathbf{w}_1, \mathbf{w}_2 \in T_{\mathbf{p}}\mathcal{M}_E, \quad (9)$$

where $d\mathbf{m}_{\mathbf{p}}$ is the differential map from the tangent space $T_{\mathbf{p}}\mathcal{M}_E$ onto the tangent space $T_{\mathbf{m}(\mathbf{p})}\mathcal{M}$ at the point $\mathbf{p} \in \mathcal{M}_E$.

2.2 | Description and discretization of curved fibers

Following Schneider,³¹ we consider a cylindrical fiber with length L and we describe its centerline by a twice continuously differentiable curve

$$\mathbf{c} : [0, L] \rightarrow Q, \quad (10)$$

where we assume a periodic rectangular unit cell $Q = [0, Q_1] \times [0, Q_2] \times [0, Q_3]$. The curve is parametrized by arc length s

$$\|\mathbf{c}'(s)\| = 1, \quad s \in [0, L], \quad (11)$$

and the diameter D is assumed to be constant, see Figure 3A. For the parametrization with the arc length, the curvature is defined as

$$\kappa(s) = \|\mathbf{c}''(s)\|. \quad (12)$$

We discretize a fiber as a polygonal chain with spherocylinders as segments.³¹ Then, a fiber consists of n segments with common segment lengths $\ell = L/n$. In the original SAM algorithm for curved fibers,³¹ every segment with index $a = 1, \dots, n$ is parametrized by its midpoint $\mathbf{x}^a \in Q$ and its direction $\mathbf{p}^a \in S^2$, where S^2 denotes the unit sphere, see Figure 3B. This parametrization appears to have $5n$ degrees of freedom. However, the condition that consecutive segments have to be connected reduces the degrees of freedom to $3 + 2n$. In the SAM algorithm,³¹ the connection of consecutive segments is ensured via penalization, which is part of the optimization method used later on.

Alternatively, the connectedness of consecutive segments may be ensured by restricting the coordinate vector

$$\mathbf{f} = \left[(\mathbf{x}^1)^T \quad \dots \quad (\mathbf{x}^n)^T \quad (\mathbf{p}^1)^T \quad \dots \quad (\mathbf{p}^n)^T \right]^T \quad (13)$$

on the configuration space

$$\mathcal{F} = \{ \mathbf{f} \in \mathbb{R}^{6n} \mid \Phi_1(\mathbf{f}) = \mathbf{0}, \Phi_2(\mathbf{f}) = \mathbf{0} \}, \quad (14)$$

where the n -dimensional vector-valued constraint function Φ_1 ensures that the directions are normed

$$\Phi_1(\mathbf{f}) = \left[\Phi_1^1(\mathbf{f}) \quad \dots \quad \Phi_1^n(\mathbf{f}) \right]^T \quad \text{with} \quad \Phi_1^a(\mathbf{f}) = \frac{1}{2} (\|\mathbf{p}^a\|^2 - 1), \quad a = 1, \dots, n, \quad (15)$$

and the $3(n-1)$ -dimensional vector-valued constraint function Φ_2 accounts for the connectedness of the fiber

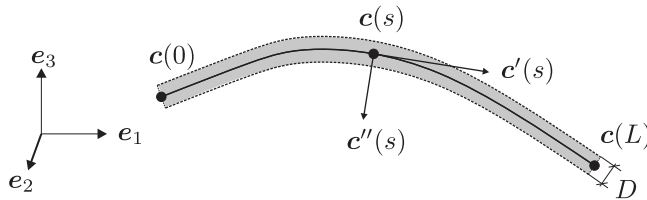
$$\Phi_2(\mathbf{f}) = \left[\Phi_2^1(\mathbf{f})^T \quad \dots \quad \Phi_2^{n-1}(\mathbf{f})^T \right]^T \quad \text{with} \quad \Phi_2^a(\mathbf{f}) = \mathbf{x}^a + \frac{\ell}{2} \mathbf{p}^a - \left(\mathbf{x}^{a+1} - \frac{\ell}{2} \mathbf{p}^{a+1} \right), \quad a = 1, \dots, n-1. \quad (16)$$

We follow this strategy for the fSAM algorithm, and aim to account for the vector-valued constraint function Φ_2 directly by the parametrization of a curved fiber. Therefore, we introduce the notation \mathbf{x}^0 for the starting point of the fiber. To obtain a completely dimensionless parametrization, we normalize the starting point with

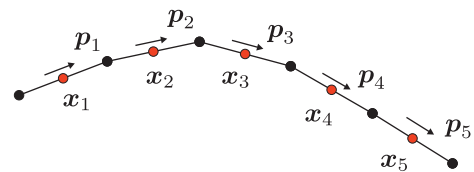
$$\hat{\mathbf{x}}^0 = \hat{\mathbf{Q}}^{-1} \mathbf{x}^0 \quad \text{with} \quad \hat{\mathbf{Q}} = \text{diag}(Q_1, Q_2, Q_3), \quad (17)$$

where the matrix $\hat{\mathbf{Q}}$ in the context of microstructure generation comprises the dimensions of the unit cell. Then, each connected polygonal chain may be parametrized via $(\hat{\mathbf{x}}^0, \mathbf{p}^1, \dots, \mathbf{p}^n) \in \mathbb{R}^3 \times (S^2)^n$. To collect the starting point and the directions of the segments in vector-valued form, we define the coordinate vector $\mathbf{q} \in \mathbb{R}^{n_q}$ as

$$\mathbf{q} = \left[(\hat{\mathbf{x}}^0)^T \quad (\mathbf{p}^1)^T \quad \dots \quad (\mathbf{p}^n)^T \right]^T \quad (18)$$



(A) Description of a curved fiber with a twice continuously differentiable curve parametrized by arc length



(B) Discretization as polygonal chain

FIGURE 3 Description of a curved fiber with a twice continuously differentiable curve parametrized by arc length (A) and discretized polygonal chain (B).

where the dimension n_q of the coordinate vector is

$$n_q = 3(n + 1). \quad (19)$$

Hence, the admissible configuration space of a polygonal chain parametrized via the vector \mathbf{q} (18) is given by the set

$$\mathcal{R} = \{ \mathbf{q} \in \mathbb{R}^{n_q} \mid \Phi_1(\mathbf{f}(\mathbf{q})) = \mathbf{0} \}, \quad (20)$$

where the coordinate vector \mathbf{f} derives from the relation

$$\begin{aligned} \mathbf{f}(\mathbf{q}) &= \left[(\mathbf{x}^1(\mathbf{q}))^T \cdots (\mathbf{x}^n(\mathbf{q}))^T (\mathbf{p}^1)^T \cdots (\mathbf{p}^n)^T \right]^T, \quad \mathbf{q} \in \mathcal{R}, \\ \text{with } \mathbf{x}^a(\mathbf{q}) &= \hat{\mathbf{Q}} \hat{\mathbf{x}}^0 + \sum_{b=1}^{a-1} \ell \mathbf{p}^b + \frac{\ell}{2} \mathbf{p}^a, \quad a = 1, \dots, n. \end{aligned} \quad (21)$$

The configuration space \mathcal{R} (20) consists of (products of) the rectangular box $[0, 1] \times [0, 1] \times [0, 1]$ (with periodic boundary conditions) for the normalized starting point $\hat{\mathbf{x}}^0$ and of the unit sphere S^2 for the directions of the segments \mathbf{p}^a . As the configuration space \mathcal{R} parametrizes the admissible configuration space for the coordinate vector $\mathbf{f} \in \mathbb{R}^{6n}$, it turns out to be a Riemannian manifold (\mathcal{R}, g) ³⁷ with a natural metric g , inherited from the known scalar product of the Euclidean space. Due to the restriction of the directions on the unit sphere, the tangent space $T_{\mathbf{q}}\mathcal{R}$ at $\mathbf{q} \in \mathcal{R}$ arises as the null space of the constraint Jacobian

$$T_{\mathbf{q}}\mathcal{R} = \text{null} \left(\frac{\partial \Phi_1(\mathbf{f}(\mathbf{q}))}{\partial \mathbf{q}} \right). \quad (22)$$

According to the derivation in Appendix A, the Riemannian metric g of the manifold \mathcal{R} is constant $g_{\mathbf{q}} \equiv g$ and given in the explicit form

$$g(\dot{\mathbf{q}}_1, \dot{\mathbf{q}}_2) = \dot{\mathbf{q}}_1^T \mathbf{G} \dot{\mathbf{q}}_2, \quad \mathbf{q} \in \mathcal{R}, \quad \dot{\mathbf{q}}_1, \dot{\mathbf{q}}_2 \in T_{\mathbf{q}}\mathcal{R}, \quad (23)$$

with the constant metric matrix

$$\mathbf{G} = \begin{bmatrix} n \hat{\mathbf{Q}}^2 & f_1 \ell \hat{\mathbf{Q}} & f_2 \ell \hat{\mathbf{Q}} & \cdots & f_n \ell \hat{\mathbf{Q}} \\ & f_{d,1} \mathbf{1}_{3 \times 3} & f_2 \ell^2 \mathbf{1}_{3 \times 3} & \cdots & f_n \ell^2 \mathbf{1}_{3 \times 3} \\ & & \ddots & & \vdots \\ & & & \ddots & f_n \ell^2 \mathbf{1}_{3 \times 3} \\ \text{sym} & & & & f_{d,n} \mathbf{1}_{3 \times 3} \end{bmatrix} \quad \text{with } f_a = n - a + \frac{1}{2} \quad \text{and} \quad f_{d,a} = \varepsilon(\ell, D) + \ell^2 \left(n - a + \frac{1}{4} \right). \quad (24)$$

Here, $\hat{\mathbf{Q}}$ denotes the normalization matrix for the starting point (17), ℓ the segment length and $\varepsilon(\ell, D)$ the volume-specific moment of inertia of a spherocylinder⁴⁰

$$\varepsilon(\ell, D) = \frac{I(\ell, D)}{V(\ell, D)} = \frac{D^2}{2/3 + \ell/D} \left[\frac{(\ell/D)^3}{12} + \frac{(\ell/D)^2}{6} + \frac{3\ell/D}{16} + \frac{1}{15} \right] \quad (25)$$

with the volume $V(\ell, D)$ and the moment of inertia $I(\ell, D)$ of a spherocylinder. For an exact expression of the moment of inertia $I(\ell, D)$, we refer to Garcia^{40(appendix B)}. To obtain Equation (25), the density of a spherocylinder is set to unity. We remark that the vectors with overdots $\dot{\mathbf{q}}_1, \dot{\mathbf{q}}_2 \in T_{\mathbf{q}}\mathcal{R}$ in Equation (23) are no time derivatives, but tangent vectors in the tangent space $T_{\mathbf{q}}\mathcal{R}$, and may be velocity vectors.

2.3 | Adapted gradient descent approach on the configuration space of curved fibers

We aim to solve an optimization problem

$$F(\mathbf{q}) \rightarrow \min_{\mathbf{q} \in \mathcal{R}} \quad (26)$$

with a gradient descent approach on the configuration space \mathcal{R} (20) with constant metric g (23), where the coordinate vector $\mathbf{q} \in \mathbb{R}^{n_q}$ is restricted to the manifold \mathcal{R} due to the vector-valued constraint function Φ_1 (15). Proceeding with the standard gradient descent on vector spaces does not respect the constraints, in general, as illustrated in Figure 2A. To compute admissible iterates, the gradient descent approach may be adapted by moving along the geodesics, that is, the shortest paths between two points on the manifold,^{36,37} see Figure 2B. According to Equation (5), a geodesic on the manifold \mathcal{R} may be obtained by minimizing the energy functional for a curve $\mathbf{q}(t) \in \mathbb{R}^{n_q}$ under the condition that the curve lies on the manifold, that is, the vector-valued constraint function $\Phi_1(\mathbf{f}(\mathbf{q}(t)))$ is the zero vector. Then, the system of equations governing the geodesic equals a constrained mechanical system given in the form of the differential-algebraic equations (DAEs) in Equation (6). For the geodesic on the manifold \mathcal{R} , an explicit form of the system of equations (6) may be derived, see Appendix B. Resulting from this derivation, the geodesics on the Riemannian manifold of curved fibers \mathcal{R} (20) is governed by

$$\begin{aligned} \mathbf{G} \ddot{\mathbf{q}}(t) + \mathbf{J}(\mathbf{q}(t))^T \lambda(t) &= \mathbf{0}, \\ \Phi_1(\mathbf{f}(\mathbf{q}(t))) &= \mathbf{0}, \end{aligned} \quad (27)$$

depending on the constant symmetric positive-definite metric matrix $\mathbf{G} \in \mathbb{R}^{n_q \times n_q}$ (24), the coordinate vector $\mathbf{q}(t) \in \mathbb{R}^{n_q}$ (18), the vector of Lagrangian multipliers $\lambda(t)$, the vector of constraints $\Phi_1(\mathbf{f}(\mathbf{q}(t))) \in \mathbb{R}^n$ (15) and the transposed Jacobian of the constraint vector $\mathbf{J}(\mathbf{q}(t))^T \in \mathbb{R}^{n_q \times n}$ in explicit form

$$\mathbf{J}(\mathbf{q}(t))^T = \begin{bmatrix} \mathbf{0}_{3 \times 1} & \mathbf{0}_{3 \times 1} & \cdots & \mathbf{0}_{3 \times 1} \\ \mathbf{p}^1(t) & \mathbf{0}_{3 \times 1} & \cdots & \mathbf{0}_{3 \times 1} \\ \mathbf{0}_{3 \times 1} & \mathbf{p}^2(t) & \cdots & \mathbf{0}_{3 \times 1} \\ \vdots & \vdots & \ddots & \vdots \\ \mathbf{0}_{3 \times 1} & \mathbf{0}_{3 \times 1} & \cdots & \mathbf{p}^n(t) \end{bmatrix}. \quad (28)$$

The coordinate vector $\mathbf{q}(t)$ and the vector of the Lagrangian multipliers $\lambda(t)$ are curves parametrized with the arc length t . To shorten the expressions, we will suppress this time-dependency further, that is, we will write

$$\lambda \equiv \lambda(t) \quad \text{and} \quad \mathbf{q} \equiv \mathbf{q}(t). \quad (29)$$

For the geodesically complete Riemannian manifold (\mathcal{R}, g) , the *exponential mapping* takes a tangent vector $\mathbf{v} \in T_{\mathbf{q}}\mathcal{R}$ and a point on the manifold $\mathbf{q} \in \mathcal{R}$ and computes

$$\exp_{\mathbf{q}}(\mathbf{v}) = \mathbf{q}_v(1), \quad (30)$$

where $\mathbf{q}_v : [0, 1] \rightarrow \mathcal{R}$ is the unique geodesic with the starting point $\mathbf{q}_v(0) = \mathbf{q}$ and the initial tangent vector $\dot{\mathbf{q}}_v(0) = \mathbf{v}$. With this insight at hand, the iterates of the gradient descent approach may be computed via the scheme

$$\mathbf{q}^{k+1} = \exp_{\mathbf{q}^k}(-\tau_k \nabla_{\mathbf{q}} F(\mathbf{q}^k)), \quad k = 0, 1, \dots, \quad (31)$$

with step size τ_k to enable an admissible optimization procedure on the Riemannian manifold \mathcal{R} .

2.4 | D'Alembert type constrained mechanical system governing the geodesics

Due to the presence of the Lagrange multipliers λ in the system of equations (27), we need to solve for $n_q + n$ unknowns, although the system has only $n_q - n$ degrees of freedom. There is a systematic procedure to reduce degrees of freedom to n_q unknowns, called *d'Alembert principle*. This strategy is based on identifying the tangent space $\dot{\mathbf{q}} \in T_{\mathbf{q}}\mathcal{R}$ at $\mathbf{q} \in \mathcal{R}$ explicitly. To do so, we differentiate the condition $\Phi_1(\mathbf{f}(\mathbf{q})) = \mathbf{0}$ with regard to the time

$$\mathbf{J}(\mathbf{q}) \dot{\mathbf{q}} = \mathbf{0}, \quad (32)$$

which uncovers that the tangent space $\dot{\mathbf{q}} \in T_{\mathbf{q}}\mathcal{R}$ at $\mathbf{q} \in \mathcal{R}$ arises as the null space of the constraint Jacobian $\mathbf{J}(\mathbf{q})$. Let the vectors $\mathbf{t}_j \in \mathbb{R}^{n_q}$ ($j = 1, \dots, n_q - n$) be a basis of the tangent space $T_{\mathbf{q}}\mathcal{R}$. Then, the *null space matrix* $\mathbf{P}(\mathbf{q}) \in \mathbb{R}^{n_q \times (n_q - n)}$ ³⁹ may be constructed such that its range, also called column space, is equal to the tangent space

$$\text{range}(\mathbf{P}(\mathbf{q})) \equiv T_{\mathbf{q}}\mathcal{R} = \text{null}(\mathbf{J}(\mathbf{q})), \quad (33)$$

using the basis vectors $\mathbf{t}_j \in \mathbb{R}^{n_q}$ as its column vectors

$$\mathbf{P}(\mathbf{q}) = \begin{bmatrix} \mathbf{t}_0 & \cdots & \mathbf{t}_{n_q - n} \end{bmatrix}. \quad (34)$$

By this construction, the null space matrix $\mathbf{P}(\mathbf{q})$ maps any vector $\mathbf{u} \in \mathbb{R}^{n_q - n}$ onto the tangent space $T_{\mathbf{q}}\mathcal{R}$ at $\mathbf{q} \in \mathcal{R}$ ³⁹

$$\mathbf{P}(\mathbf{q}) : \mathbb{R}^{n_q - n} \rightarrow T_{\mathbf{q}}\mathcal{R}. \quad (35)$$

For an arbitrary basis of the tangent space $T_{\mathbf{q}}\mathcal{R}$, the linear mapping in Equation (35) is not isometric, in general. To preserve the size of the vector \mathbf{u} , we require that the null space matrix is an isometry, that is, its column vectors correspond to an orthonormal basis.⁴¹ Then, every tangent vector $\mathbf{v} \in T_{\mathbf{q}}\mathcal{R}$ may be parametrized in the space $\mathbb{R}^{n_q - n}$ with the vector

$$\mathbf{u} = \mathbf{P}^T \mathbf{v} \quad (36)$$

and the condition $\mathbf{v} = \mathbf{P} \mathbf{u}$ holds. Betsch³⁹ derives an explicit formulation for the isometric null space matrix of the double spherical pendulum. Extending this formulation to the considered polygonal chain leads to

$$\mathbf{P}(\mathbf{q}) = \begin{bmatrix} \mathbf{1}_{3 \times 3} & \mathbf{0}_{3 \times 3} & \cdots & \mathbf{0}_{3 \times 3} \\ \mathbf{0}_{3 \times 2} & \mathbf{P}^1(\mathbf{p}^1) & \cdots & \mathbf{0}_{3 \times 2} \\ \vdots & \vdots & \ddots & \vdots \\ \mathbf{0}_{3 \times 2} & \mathbf{0}_{3 \times 2} & \cdots & \mathbf{P}^n(\mathbf{p}^n) \end{bmatrix} \quad \text{with} \quad \mathbf{P}^a(\mathbf{p}^a) = \begin{bmatrix} \mathbf{r}^a(\mathbf{p}^a) & \mathbf{s}^a(\mathbf{p}^a) \end{bmatrix}, \quad (37)$$

where the column vectors of the submatrices $\mathbf{P}^a(\mathbf{p}^a)$ characterize the tangent space for each segment direction

$$\begin{aligned} \mathbf{r}^a(\mathbf{p}^a) &= \mathbf{R}^a \mathbf{e}_1, & \mathbf{s}^a(\mathbf{p}^a) &= \mathbf{R}^a \mathbf{e}_2 \\ \text{with } \mathbf{R}^a &= (\mathbf{e}_3 \cdot \mathbf{p}^a) \mathbf{1}_{3 \times 3} + (\mathbf{e}_3 \times \mathbf{p}^a) \times + \frac{(\mathbf{e}_3 \times \mathbf{p}^a) \otimes (\mathbf{e}_3 \times \mathbf{p}^a)}{1 + \mathbf{e}_3 \cdot \mathbf{p}^a}. \end{aligned} \quad (38)$$

Here, the formulation $(\mathbf{e}_3 \times \mathbf{p}^a) \times$ denotes a skew-symmetric matrix with corresponding axial vector $\mathbf{e}_3 \times \mathbf{p}^a$, see Section 1.3. As the null space matrix $\mathbf{P}(\mathbf{q})$ is constructed such that the product $\mathbf{P}(\mathbf{q})^T \mathbf{J}(\mathbf{q})$ is a zero matrix, the equivalent form of Equation (27)

$$\begin{aligned} \mathbf{P}(\mathbf{q})^T \mathbf{G} \ddot{\mathbf{q}} &= \mathbf{0}, \\ \Phi_1(\mathbf{f}(\mathbf{q})) &= \mathbf{0}, \end{aligned} \quad (39)$$

leads to a system of equation with n_q unknowns.

2.5 | Numerical integration of the d'Alembert type constrained mechanical system

For the numerical integration of Equation (39), we follow Betsch³⁹ and use the energy conserving time integration scheme introduced by Gonzales.⁴² We briefly introduce the main aspects of the numerical integration scheme, especially with respect to the considered use case. For more details, we refer to Betsch.³⁹

We are interested in the evolution of the coordinate vector \mathbf{q} in the time interval $I = [0, 1]$. For the numerical integration, we divide the time interval I into n_t subintervals of length $\Delta t = 1/n_t$. On a single time interval $I_j = [t_j, t_{j+1}]$, we approximate the coordinate vector and its first time derivative via

$$\begin{aligned}\mathbf{q}(t) &\approx \mathbf{q}_j + \frac{t - t_j}{\Delta t} (\mathbf{q}_{j+1} - \mathbf{q}_j), \\ \dot{\mathbf{q}}(t) &\approx \mathbf{v}_j + \frac{t - t_j}{\Delta t} (\mathbf{v}_{j+1} - \mathbf{v}_j),\end{aligned}\quad (40)$$

with given quantities $\mathbf{q}_j \in \mathcal{R}$ and $\mathbf{v}_j \in \mathbb{R}^{n_q}$ at time node t_j . To obtain the coordinate vector at time node t_{j+1} , we solve the discretized differential-algebraic equations

$$\begin{aligned}\mathbf{P}(\mathbf{q}_j, \mathbf{q}_{j+1})^T \mathbf{H}(\mathbf{q}_j, \mathbf{q}_{j+1}) &= \mathbf{0}, \\ \Phi_1(\mathbf{f}(\mathbf{q}_{j+1})) &= \mathbf{0}, \\ \text{with } \mathbf{H}(\mathbf{q}_j, \mathbf{q}_{j+1}) &= \frac{2}{\Delta t} \mathbf{G}[\mathbf{q}_{j+1} - \mathbf{q}_j] - 2 \mathbf{G} \mathbf{v}_j,\end{aligned}\quad (41)$$

via a Newton scheme, see Betsch.³⁹ $\mathbf{P}(\mathbf{q}_j, \mathbf{q}_{j+1})$ denotes the discrete null space matrix and characterizes the null space of the discrete constraint Jacobian $\mathbf{J}(\mathbf{q}_j, \mathbf{q}_{j+1})$. In general, the discrete constraint Jacobian is defined via discrete derivatives,⁴³ see Betsch.³⁹ For the special case of quadratic constraint function, for example, as for the considered polygonal chain, the discrete constraint Jacobian simplifies and is equal to the constraint Jacobian evaluated at the coordinate vector at the midpoint of the time interval $\mathbf{q}_{j+\frac{1}{2}}$

$$\mathbf{J}(\mathbf{q}_j, \mathbf{q}_{j+1}) = \mathbf{J}(\mathbf{q}_{j+\frac{1}{2}}). \quad (42)$$

Accordingly, the discrete null space matrix $\mathbf{P}(\mathbf{q}_j, \mathbf{q}_{j+1})$ equals the null space matrix $\mathbf{P}(\mathbf{q}_{j+\frac{1}{2}})$. As the starting point for the Newton iteration, the coordinate vector at time node t_{j+1} is set to

$$\mathbf{q}_{j+1} = \mathbf{q}_j + \Delta t \mathbf{v}_j. \quad (43)$$

After solving for the coordinate vector \mathbf{q}_{j+1} , the velocity is updated

$$\mathbf{v}_{j+1} = \frac{2}{\Delta t} (\mathbf{q}_{j+1} - \mathbf{q}_j) - \mathbf{v}_j, \quad (44)$$

such that all necessary quantities for the next time step are known.

With respect to the iterative Newton scheme, integrating the d'Alembert type scheme (39) instead of the basic constrained scheme (27) offers an additional advantage in terms of the conditioning of the iteration matrix. Whereas the basic scheme suffers from an ill-conditioned iteration matrix for small time steps, the condition number of the iteration matrix is independent of the time step for the d'Alembert type scheme.

In our implementation, we initially consider $n_t = 1$ subintervals of the full interval I , subdividing the considered interval whenever the Newton scheme fails to converge. As convergence criterion for the Newton scheme, we choose that the norm of the residual vector is below 10^{-4} . If more than ten Newton iterations are necessary, we stop the Newton scheme and restart the time integration with halved time steps. To ensure convergence, we apply the backtracking strategy⁴⁴ with parameters $\alpha = 1/3$ and $\beta = 0.9$. A pseudo-code for the numerical integration of the d'Alembert type constrained mechanical system is given in Algorithm 1.

3 | MICROSTRUCTURE GENERATION FOR LONG FIBER-REINFORCED COMPOSITES

3.1 | Description of long fiber reinforced composites

We consider a rectangular cell $Q = [0, Q_1] \times [0, Q_2] \times [0, Q_3]$ containing N curved fibers of constant diameter D in a non-penetrating fiber arrangement. The i^{th} -fiber is discretized as a polygonal chain, see Section 2.2. The number of segments n_i is chosen such that the segment length ℓ_i is below a defined maximum segment length $\bar{\ell}$

Algorithm 1. Numerical integration of the d'Alembert type constrained mechanical system

Input: $\mathbf{q}_1, \mathbf{v}_1$

- 1: $n_t \leftarrow 1, \Delta t \leftarrow 1$
- 2: **for** $j \leftarrow 1$ **to** n_t **do**
- 3: Initial update of the coordinate vector \mathbf{q}_{j+1} ▷ *Equation (43)
- 4: Computation of the residual vector
- 5: **while** norm of residual vector $> 10^{-4}$ **do**
- 6: **if** $j > 10$ **then**
- 7: $n_t \leftarrow 2n_t, \Delta t \leftarrow \frac{1}{2}\Delta t$
- 8: Return to line 2
- 9: Newton step with backtracking
- 10: Computation of the residual vector

$$n_i = \left\lceil \frac{L_i}{\ell} \right\rceil, \quad \ell_i = \frac{L_i}{n_i}, \quad (45)$$

where the type $\lceil \cdot \rceil$ denotes the smallest integer larger or equal to a given real number. The location of the fiber is defined by the coordinate vector \mathbf{q}_i (18). As we consider a nonpenetrating fiber arrangement, the fiber volume fraction computes as

$$\phi = \frac{\pi D^2}{4Q_1 Q_2 Q_3} L_{\text{total}} \quad \text{with the total length} \quad L_{\text{total}} = \sum_{i=1}^N L_i, \quad (46)$$

which is identical to the formula for straight cylinders.⁴⁵

For fiber-reinforced composites, it is convenient to use volume-weighted fiber orientation tensors^{46,47} as compact characteristics for the fiber orientation distribution. In case of a finite number of curved fibers, the realized volume-weighted fiber orientation tensor of second order \mathbf{A}^r and of fourth order \mathbb{A}^r compute as

$$\mathbf{A}^r = \frac{1}{L_{\text{total}}} \sum_{i=1}^N \sum_{a=1}^{n_i} \ell_i (\mathbf{p}_i^a)^{\otimes 2}, \quad \mathbb{A}^r = \frac{1}{L_{\text{total}}} \sum_{i=1}^N \sum_{a=1}^{n_i} \ell_i (\mathbf{p}_i^a)^{\otimes 4} \quad (47)$$

in tensorial notation. Typically, the fiber orientation tensors of second order \mathbf{A}^r are obtained from micro-CT scans.^{48–50} However, to predict the effective properties accurately also the fiber orientation tensor of fourth order \mathbb{A}^r is necessary.^{27,51,52} To obtain an adequate fourth order orientation tensor, closure approximations are applied.^{27,53–58} In this manuscript, we use the exact closure (ACG).^{59,60}

3.2 | Fused sequential addition and migration (fSAM) algorithm

In its original form, the sequential addition and migration (SAM)²⁴ algorithm is a method for generating periodic microstructures of short straight fiber-reinforced composites with constant lengths. Additionally, extensions of the basic scheme enable to account for fiber length distributions²⁵ and long curved fibers discretized as polygonal chains.³¹ Microstructure generation with the SAM algorithm proceeds in consecutive steps until the desired fiber volume fraction is reached. For each step, a specified amount of fibers is added randomly to the cell first. Then, an optimization framework is used, converging provided no overlap between fibers is detected and further criteria, for example, realization of the prescribed fiber orientation tensor \mathbb{A} up to the defined numerical precision, are fulfilled. Considering the extension of the SAM algorithm for long fibers,³¹ convergence problems occur as the coherence of adjacent fiber segments is not intrinsically ensured with the fiber parametrization but with an additional penalty term. In order to enable packings with higher fiber volume fractions for longer fibers, in this work we introduce the fused sequential addition and migration

(fSAM) algorithm as alternative approach to the SAM algorithm with respect to a fused fiber description and movement, see Section 2.

Therefore, we adapt the objective function introduced by Schneider³¹ to

$$F(\mathbf{f}_1, \dots, \mathbf{f}_N) \triangleq \frac{1}{2} \sum_{i,j=1}^N \sum_{a=1}^{n_i} \sum_{b=1}^{n_j} (\delta_{ij}^{ab})^2 + \frac{w_{\mathbb{A}}}{8} N \|\mathbb{A} - \mathbb{A}^r\|^2 + \frac{w_{\rho}}{2} \sum_{i=1}^N \sum_{a=1}^{n_i-1} (\rho_i^a)^2 \quad (48)$$

with weights $w_{\mathbb{A}}$ and w_{ρ} , where \mathbf{f}_i denotes the vector of all midpoints and directions of the i^{th} -fiber (18). For the SAM algorithm,³¹ an additional term for the coherence between segments is considered, which we leave out as we intrinsically fulfill this condition. The first term captures the nonoverlap condition with the quantity

$$\delta_{ij}^{ab} \equiv \left\langle D - \min_{s_i^a, s_j^b \in [-1,1]} d_Q \left(\mathbf{x}_i^a + s_i^a \frac{\ell_i}{2} \mathbf{p}_i^a, \mathbf{x}_j^b + s_j^b \frac{\ell_j}{2} \mathbf{p}_j^b \right) \right\rangle_{+} \equiv \langle D - \|\mathbf{k}_{ij}^{ab}\| \rangle_{+}, \quad (49)$$

where the vector \mathbf{k}_{ab}^{ij} relates to the smallest periodic distance between two segments and the Macaulay bracket $\langle h \rangle_{+} = \max(0, h)$ are used. The second term of $F(\mathbf{f}_1, \dots, \mathbf{f}_N)$ in Equation (48) accounts for the prescribed fiber orientation tensor. As extremely wide angles between segments are unrealistic, the third term of $F(\mathbf{f}_1, \dots, \mathbf{f}_N)$ in Equation (48) aims to limit the maximum bending angle to the prescribed value $\bar{\alpha}$ with the quantity

$$\rho_i^a \equiv \langle \cos \bar{\alpha} - \mathbf{p}_i^{a+1} \cdot \mathbf{p}_i^a \rangle_{+}. \quad (50)$$

Let us discuss the weights $w_{\mathbb{A}}$ and w_{ρ} . As the function $F(\mathbf{f}_1, \dots, \mathbf{f}_N)$ has dimension (length)² due to the first term, both weights are required to have dimension (length)² as well. Following Schneider,³¹ we choose $w_{\rho} = 0.75 \varepsilon(\ell_i, D)$, where $\varepsilon(\ell_i, D)$ is the volume-specific moment of inertia of a spherocylinder, see Equation (25). For the weight $w_{\mathbb{A}}$, Schneider³¹ uses $w_{\mathbb{A}} = \varepsilon(\ell_i, D)$. However, we observed that the fSAM algorithm and its numerical integration leads to slow convergence of the orientation condition for an increased number of segments. Hence, we choose the weight $w_{\mathbb{A}}$ to depend on the number of segments via the relation

$$w_{\mathbb{A}} \equiv \varepsilon(\ell_i, D) \frac{\varepsilon(n_i \ell_i, D)}{n_i \varepsilon(\ell_i, D)} = \frac{\varepsilon(n_i \ell_i, D)}{n_i}. \quad (51)$$

In case of a fiber consisting of a single segment, the weight $w_{\mathbb{A}}$ coincides with the SAM algorithm.

We aim to solve the optimization problem with a gradient descent approach parametrized by the coordinate vectors \mathbf{q}_i

$$F(\mathbf{f}_1, \dots, \mathbf{f}_N) \rightarrow \min_{\mathbf{q}_i \in \mathcal{R}}. \quad (52)$$

Therefore, we need to compute the respective directional derivatives of the objective function. However, the objective function $F(\mathbf{f}_1, \dots, \mathbf{f}_N)$ in Equation (48) is given in terms of the midpoints and the directions collected in the coordinate vectors \mathbf{f}_i . For this parametrization, the directional derivatives are computed via

$$\begin{aligned} \frac{\partial F(\mathbf{f}_1, \dots, \mathbf{f}_N)}{\partial \mathbf{x}_i^a} &\triangleq - \sum_{j=1}^N \sum_{b=1}^{n_j} \delta_{ij}^{ab} \frac{\mathbf{k}_{ij}^{ab}}{\|\mathbf{k}_{ij}^{ab}\|}, \\ \frac{\partial F(\mathbf{f}_1, \dots, \mathbf{f}_N)}{\partial \mathbf{p}_i^a} &\triangleq - \sum_{j=1}^N \sum_{b=1}^{n_j} \delta_{ij}^{ab} \frac{\ell_i s_{ij}^{ab}}{2} \frac{\mathbf{k}_{ij}^{ab}}{\|\mathbf{k}_{ij}^{ab}\|} - w_{\mathbb{A}} \frac{\ell_i N}{L_{\text{total}}} (\mathbb{A} - \mathbb{A}^r) [(\mathbf{p}_i^a \otimes \mathbf{p}_i^a)^3] - w_{\rho} (\rho_i^a \mathbf{p}_i^{a+1} + \rho_i^{a-1} \mathbf{p}_i^{a-1}), \end{aligned} \quad (53)$$

according to the SAM algorithm for curved fibers.³¹ To obtain the directional derivatives for the coordinate vectors \mathbf{q}_i from Equation (53), we have to account for the dependence between these two parametrizations, see Equation (21). Then, we obtain the relation

$$\frac{\partial F(\mathbf{f}_1, \dots, \mathbf{f}_N)}{\partial \mathbf{q}_i} = \left(\frac{\partial \mathbf{f}_i}{\partial \mathbf{q}_i} \right)^T \frac{\partial F(\mathbf{f}_1, \dots, \mathbf{f}_N)}{\partial \mathbf{f}_i}$$

$$= \begin{bmatrix} \hat{\mathbf{Q}} \sum_{a=1}^{n_i} \frac{\partial F(\mathbf{f}_1, \dots, \mathbf{f}_N)}{\partial \mathbf{x}_i^a} \\ R_1(\mathbf{f}_1, \dots, \mathbf{f}_N) \\ \vdots \\ R_{n_i}(\mathbf{f}_1, \dots, \mathbf{f}_N) \end{bmatrix} \quad (54)$$

$$\text{with } R_a(\mathbf{f}_1, \dots, \mathbf{f}_N) = F(\mathbf{f}_1, \dots, \mathbf{f}_N) \left(\frac{\partial}{\partial \mathbf{p}_i^a} + \sum_{b=a+1}^{n_i} \ell_i \frac{\partial}{\partial \mathbf{x}_i^b} + \frac{\ell_i}{2} \frac{\partial}{\partial \mathbf{x}_i^a} \right),$$

where $\hat{\mathbf{Q}}$ denotes the normalization matrix for the starting point (17) and ℓ_i the segment length.

For Riemannian manifolds, the gradient computes as the linear map of the directional derivatives by the inverse of the metric matrix.³⁷ Hence, the gradient of the objective function $F(\mathbf{f}_1, \dots, \mathbf{f}_N)$ with respect to the coordinate vectors \mathbf{q}_i follows as

$$\nabla_{\mathbf{q}_i} F(\mathbf{f}_1, \dots, \mathbf{f}_N) = \mathbf{G}_i^{-1} \frac{\partial F(\mathbf{f}_1, \dots, \mathbf{f}_N)}{\partial \mathbf{q}_i} \quad (55)$$

with the metric matrix \mathbf{G}_i (24), which differs throughout the polygonal chains in case the segment lengths ℓ_i or the numbers of segments n_i are not constant.

As the motion is restricted to a curved manifold, a basis descent gradient approach may leave the optimization space, see Figure 2A. To ensure a motion on the manifold, we compute the iterates of the gradient descent approach moving along the geodesics and account for the periodicity with respect to the normalized starting points. This iterative procedure may be written in the form

$$\mathbf{q}_i^{k+1} = \exp_{\mathbf{q}_i^k} \left(-\tau \nabla_{\mathbf{q}_i} F(\mathbf{f}_1^k, \dots, \mathbf{f}_N^k) \right), \quad k = 0, 1, \dots, \quad (56)$$

where τ denotes the stepsize and $\exp_{\mathbf{q}}(\mathbf{v})$ refers to the exponential mapping, see Equation (2.29), with a tangent vector $\mathbf{v} \in T_{\mathbf{q}}\mathcal{R}$ and a point on the manifold $\mathbf{q} \in \mathcal{R}$. The exponential mapping is realized by numerically integrating the d'Alembert type mechanical constrained system, explained in Section 2.5, using the point $\mathbf{q} \in \mathcal{R}$ and the tangent vector $\mathbf{v} \in T_{\mathbf{q}}\mathcal{R}$ as initial condition at time $t_0 = 0$. As the exponential mapping of a single fiber's coordinate vector is independent of the remaining fibers, the numerical integration may be computed independently for each fiber, thus, the computation may be parallelized directly. We select the stepsize $\tau = 0.501$.²⁴ Additionally, we multiply the directional derivatives $\partial F(\mathbf{f}_1^k, \dots, \mathbf{f}_N^k) / \partial \mathbf{p}_i^a$ with the stepsize $\tau_p = 0.3$ to prefer translation over rotation, following the SAM algorithm.²⁴ A pseudo-code for a single iterative optimization step of the fSAM algorithm is given in Algorithm 2.

Algorithm 2. Iterative optimization step of the fSAM algorithm

Input: Coordinate vector \mathbf{q}_i^k , $i = 1, \dots, n$

- 1: Compute the coordinate vectors \mathbf{f}_i^k ▷ *Equation (21)
 - 2: **for** $i \leftarrow 1$ **to** n **do**
 - 3: **for** $a \leftarrow 1$ **to** n_i **do**
 - 4: Compute the directional derivatives $\frac{\partial F(\mathbf{f}_1^k, \dots, \mathbf{f}_N^k)}{\partial \mathbf{x}_i^a}$ and $\frac{\partial F(\mathbf{f}_1^k, \dots, \mathbf{f}_N^k)}{\partial \mathbf{p}_i^a}$ ▷ *Equation (53)
 - 5: Compute the directional derivative $\frac{\partial F(\mathbf{f}_1^k, \dots, \mathbf{f}_N^k)}{\partial \mathbf{q}_i}$ ▷ *Equation (54)
 - 6: Compute the gradient $\nabla_{\mathbf{q}_i} F(\mathbf{f}_1^k, \dots, \mathbf{f}_N^k)$ ▷ *Equation (55)
 - 7: Compute the updated coordinate vector \mathbf{q}_i^{k+1} ▷ *Equation (56) following Sections (2.3) to (2.5)
-

When computing the gradients with Equation (53), most of the time/effort is spent for the evaluation of the inter-segment distances. To generate periodic microstructures, we use periodic distances between the fiber segments. Assuming the fiber segments are smaller than the half of the minimum of the cell dimensions Q_i , the periodic distance between two points $\mathbf{x}, \mathbf{y} \in Q$ may be computed as

$$d_Q(\mathbf{x}, \mathbf{y}) = \sqrt{\sum_{i=1}^3 (\mathcal{P}((\mathbf{x} - \mathbf{y}) \cdot \mathbf{e}_i, Q_i))^2}, \quad \mathbf{x}, \mathbf{y} \in Q, \quad (57)$$

with the function

$$\mathcal{P}(\xi, L) = \begin{cases} \xi - L, & \text{for } \xi > L/2, \\ \xi + L, & \text{for } \xi \leq -L/2, \\ \xi, & \text{else,} \end{cases} \quad (58)$$

see Schneider.³¹ To reduce the effort, two main aspects need to be considered. First, a fast computation of the periodic distances is necessary. Therefore, we use a modified Vega-Lago algorithm⁶¹ introduced in Pournin et al.⁶² Additionally, the number of distance measurements should be reduced. To check only close segments for collision, we use cell-linked lists⁶³ in combination with nested Verlet lists.^{24,64} For more details on the implementation of these strategies for the distance computation, we refer to previous publications on the SAM algorithm.^{24,25,31}

3.3 | Gamma distribution as fiber length distribution

Due to the manufacturing processes of fiber-reinforced composites, the fiber lengths vary throughout the component. For short fiber-reinforced composites, Mehta and Schneider²⁵ show the importance of capturing the varying fiber lengths when computing the effective properties with minimum effort. As for long fiber reinforced composites the fiber lengths are even more varying,^{30,34,35} we aim to realize the fiber lengths adequately.

Typically, only the volume-weighted mean m and standard deviation s are available as statistic quantities measured in experiments. To model a fiber length distribution with these input parameters, a distribution type has to be chosen which captures the main characteristics of the measured fiber length distributions. In case of long-fiber reinforced polymers, the fiber length distribution involves a monotonically decreasing curve and high standard deviations.^{30,34,35} To model such a qualitative behavior, the Gamma distribution may be used, see Figure 4, which is defined via the probability density function

$$\rho_{\alpha,\beta}(L) = \frac{\beta^\alpha}{\Gamma(\alpha)} L^{\alpha-1} \exp(-\beta L), \quad L > 0, \quad (59)$$

depending on the shape parameter $\alpha > 0$ and the rate parameter $\beta > 0$.

For the problem at hand, we need to compute the distribution parameters α and β from the volume-weighted mean m and the standard deviation s . Provided the volume of the considered objects only varies due to the length, for example, as it holds for straight cylinders with constant diameter, Mehta and Schneider^{25(Apx. A)} derive the conditions

$$m = \frac{\langle \ell^2 \rangle}{\langle \ell \rangle}, \quad s^2 = \frac{\langle \ell^3 \rangle}{\langle \ell \rangle} - m^2, \quad (60)$$

where the notation $\langle Z \rangle$ is used for the expectation of the random variable Z . As the volume of a curved cylindrical fiber with constant diameter D coincides with the volume of a straight cylindrical fiber with equal diameter,⁴⁵ the condition (60) holds for the considered polygonal chain. For a random variable Z following the Gamma distribution with distribution parameters α and β , the expectation of the n^{th} -power of the random variable Z is given by the expression⁶⁵

$$\langle Z^n \rangle = \frac{1}{\beta^n} \prod_{i=1}^n (\alpha + i - 1), \quad n \in \mathbb{N}. \quad (61)$$

With the expression (61) at hand, we reformulate Equation (60) to get the system

$$m = \frac{\alpha + 1}{\beta}, \quad s^2 = \frac{\alpha + 1}{\beta^2} \quad (62)$$

of equations. Solving for α in the first equation and inserting this expression into the second equation yields the explicit relations

$$\alpha = \frac{m^2}{s^2} - 1, \quad \beta = \frac{m}{s^2}. \quad (63)$$

Due to the asymptotic behavior of the Gamma distribution for high standard deviations shown in Figure 4, sampling from the Gamma distribution results in numerous fibers with unrealistically small fiber lengths. To overcome this limitation, we only consider fiber lengths exceeding a chosen minimum fiber length. Attention has to be taken that the minimum fiber length is small enough such that the volume-weighted quantities are not influenced significantly. Hence, we choose the minimum fiber length to be equal to the fiber diameter such that also the smallest fiber length is larger than the diameter.

For an accurate realization of the statistic quantities m and s , it is critical to select an adequate sampling strategy, especially when considering high standard deviations as in long fiber reinforced polymers. Due to the advantages of a sampling strategy with scrambled Sobol sequences^{66,67} compared to a classic Monte Carlo approach,⁶⁸ see Mehta and Schneider,²⁵ we use this scheme for the fiber length sampling.

Besides the Gamma distribution, also other distribution types may be used to model the fiber length distribution of long fiber reinforced polymers, for example, the Beta, Weibull or log-normal distribution. For the material at hand, the Gamma distribution turns out to be a sufficiently accurate model for the fiber length distribution.

3.4 | Handling of extremely long fibers

If the fiber lengths are sampled from a fiber length distribution, for example, the Gamma distribution, extremely long fibers with high numbers of segments n may be present. For the numerical integration of the fiber movement, systems of linear equations of a dimension $n_q = 3(n_i + 1)$ need to be solved. As the effort of direct solvers scales cubically in n_q , it may be extremely time-consuming to determine the fiber movement for fibers with many segments.

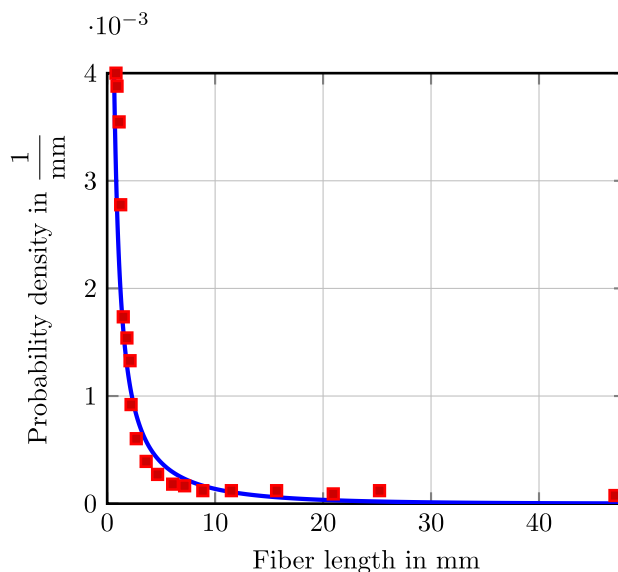


FIGURE 4 Gamma distribution with volume-weighted mean $m = 15.00$ mm and standard deviation $s = 14.98$ mm (blue), fitted to fiber length data of a PPGF30 material³⁰ (red).

To improve the efficiency for increasing aspect ratios, we introduce a *mixed* procedure which combines the advantages of the SAM and fSAM algorithm. If more segments than a prescribed maximum number \bar{n} are necessary, then the fiber will be divided in

$$n_p = \left\lceil \frac{n_i}{\bar{n}} \right\rceil \quad (64)$$

polygonal chains, which will move separately. The first $n_p - 1$ chains comprise \bar{n} -segments each, and the last chain collects the remaining segments. To illustrate the separation into multiple chains, a fiber with $n = 15$ segments and a maximum number of segments $\bar{n} = 6$ is shown in Figure 5. The distance between adjacent chains is highlighted by the two dashed connection lines.

With the introduced separation, we satisfy the coherence condition for the links in each subchain but not between *different* subchains, see Figure 5. However, we still require that the coherence is a convergence criterion for the optimization process. To overcome this issue, we account for an additional term in the optimization function with respect to the coherence criterion,³¹ which we have left out in Equation (48)

$$F(\mathbf{f}_1, \dots, \mathbf{f}_N) \hat{=} \frac{1}{2} \sum_{i=1}^N \sum_{a=1}^{n_i} \sum_{b=1}^{n_j} (\delta_{ij}^{ab})^2 + \frac{w_{\mathbb{A}}}{8} N \|\mathbb{A} - \mathbb{A}^r\|^2 + \frac{w_{\rho}}{2} \sum_{i=1}^N \sum_{a=1}^{n_i-1} (\rho_i^a)^2 + \frac{w_{\gamma}}{2} \sum_{i=1}^N \sum_{a=1}^{n_i-1} (\gamma_i^a)^2. \quad (65)$$

The quantity γ_a^i is defined as the smallest periodic distance between two adjacent segments. As we still fulfill the coherence condition within the chains intrinsically, the quantity γ_a^i is only nonzero for adjacent segments which are part of two different subchains. Hence, the quantity γ_a^i may be computed via

$$\gamma_i^a \equiv \begin{cases} d_Q \left(\mathbf{x}_i^a + \frac{\ell_i}{2} \mathbf{p}_i^a, \mathbf{x}_i^{a+1} - \frac{\ell_i}{2} \mathbf{p}_i^{a+1} \right), & \text{if } a \in \{\bar{n}, 2\bar{n}, 3\bar{n}, \dots\} \\ 0, & \text{else} \end{cases}, \quad a = 1, \dots, n_i - 1. \quad (66)$$

As the fourth term in Equation (65) needs to have dimension (length)², the weight w_{γ} is dimensionless, and we choose $w_{\gamma} = 0.75$.³¹ Due to the additional term in the objective function, also the directional derivatives extend

$$\begin{aligned} \frac{\partial F(\mathbf{f}_1, \dots, \mathbf{f}_N)}{\partial \mathbf{x}_i^a} &\hat{=} - \sum_{j=1}^N \sum_{b=1}^{n_j} \delta_{ij}^{ab} \frac{\mathbf{k}_{ij}^{ab}}{\|\mathbf{k}_{ij}^{ab}\|} + w_{\gamma} (\mathbf{v}_i^a - \mathbf{v}_i^{a+1}), \\ \frac{\partial F(\mathbf{f}_1, \dots, \mathbf{f}_N)}{\partial \mathbf{p}_i^a} &\hat{=} - \sum_{j=1}^N \sum_{b=1}^{n_j} \delta_{ij}^{ab} \frac{\ell_i s_{ij}^{ab}}{2} \frac{\mathbf{k}_{ij}^{ab}}{\|\mathbf{k}_{ij}^{ab}\|} - w_{\mathbb{A}} \frac{\ell_i N}{L_{\text{total}}} (\mathbb{A} - \mathbb{A}^r) [(\mathbf{p}_i^a) \otimes^3] - w_{\rho} (\rho_i^a \mathbf{p}_i^{a+1} + \rho_i^{a-1} \mathbf{p}_i^{a-1}) + \frac{w_{\gamma} \ell_i}{2} (\mathbf{v}_i^a + \mathbf{v}_i^{a+1}), \end{aligned} \quad (67)$$

where the vector \mathbf{v}_i^a relates to the smallest periodic distance between two adjacent segments.

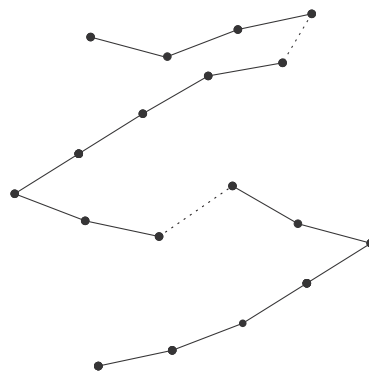


FIGURE 5 Separation of a fiber with $n = 15$ segments and a maximum number of segments $\bar{n} = 6$ into three chains.

Attention has to be taken that the maximum number of segments \bar{n} is chosen adequately. On the one hand, if the parameter is too small, convergence problems due to the coherence condition will arise similar to the SAM algorithm. On the other hand, if the maximum number of segments is too large, the runtime for the numerical integration will increase drastically.

4 | COMPUTATIONAL INVESTIGATIONS

4.1 | Setup

For the computational investigations, we use an implementation of the fSAM algorithm in Python with Cython extensions. This implementation features parallelization with OpenMP for collision checks between the fibers and the numerical integration of the fiber movement. The measured runtimes were recorded on a desktop computer with a 8-core Intel i7 CPU and 64GB RAM.

We consider the material parameters of a polypropylene (PP) matrix reinforced by E-glass fibers,^{69,70} see Table 1. As our reference setup, we model the fibers with a diameter of $D = 17 \mu\text{m}$. We restrict the segment lengths to $\bar{\ell} = 100 \mu\text{m}$ and the maximum angles to $\bar{\alpha} = 60^\circ$. To avoid stress peaks for fibers which are too close,^{71,72} we enforce a minimum inter-fiber distance of 20% of the fiber diameter, that is, for a diameter of $D = 17 \mu\text{m}$ the minimum distance is $3.4 \mu\text{m}$. The fiber lengths, the fiber volume fraction and the fiber orientation tensor vary throughout the different studies. As the reference algorithm, we use the pure fSAM algorithm, introduced in Section 3.2. Only for the computational studies in the Sections 4.5 and 4.7, we also use the mixed procedure with a maximum segment number of $\bar{n} = 20$, see Section 3.4. For the pure fSAM algorithm and the mixed procedure, we add the fibers which are necessary to reach the desired fiber volume fractions in a single step.

To reduce boundary effects, we generate periodic microstructures. From a computational point of view, this requirement manifests in periodic distance computations between the individual fiber segments. The fiber orientation tensors of fourth order are approximated with the exact closure by a prescribed fiber orientation tensor of second order. As termination criteria for the microstructure generation with the fSAM algorithm, we enforce that the nonoverlapping condition is fulfilled strictly. Additionally, the fiber orientation tensor has to be realized with a relative error below 10^{-4} and the angle constraint with an absolute error below 10^{-2} . In case of the mixed procedure, the termination criterion for the coherence condition is a distance between adjacent chains below $10^{-3}D$, where D denotes the fiber diameter.

The effective elastic properties are computed with FFT-based computational homogenization software.^{73,74} We use a discretization on a staggered grid⁷⁵ and a conjugate gradient solver^{76,77} with a relative tolerance of 10^{-5} as termination criterion. Based on six independent load cases, we first compute the effective elasticity tensor. Second-order fiber orientation tensors are always orthotropic.^{78,79} Hence, also the fiber orientation tensors of fourth order approximated by the exact closure are at most orthotropic.⁵² For this reason, we report on the effective orthotropic engineering constants approximated from the full effective elastic tensor.^{78,80}

4.2 | On the difference between the SAM and the fSAM algorithm

The main goals of the extension towards a fused fiber movement are, on the one hand, to enable faster microstructure generation and, on the other hand, to achieve packings with high fiber volume fractions for long fibers. To assess the improvement, we start our investigations by comparing the efficiency of the microstructure generation for both the SAM and the fSAM algorithm. For this purpose, we generate microstructures with a cubic unit cell and cell dimension $Q_i = 748 \mu\text{m}$. The fibers are modeled with a uniform fiber length of $L = 1700 \mu\text{m}$, that is, a fiber aspect ratio of $r_a = 100$. For the study, we consider the fiber volume fractions

TABLE 1 Material properties for the PP matrix and the E-glass fibers.^{69,70}

E-glass fibers	PP matrix
$E = 72.0 \text{ GPa}$	$E = 1.25 \text{ GPa}$
$\nu = 0.22$	$\nu = 0.35$

$$\phi \in \{5\%, 10\%, 15\%, 20\%\} \quad (68)$$

and the second-order fiber orientation tensors

$$\begin{aligned} \mathbf{A}_1 &\hat{=} \text{diag}(0.33, 0.33, 0.33), & \mathbf{A}_2 &\hat{=} \text{diag}(0.48, 0.48, 0.04), \\ \mathbf{A}_3 &\hat{=} \text{diag}(0.96, 0.02, 0.02), & \mathbf{A}_4 &\hat{=} \text{diag}(0.77, 0.17, 0.06), \end{aligned} \quad (69)$$

where the last fiber orientation corresponds to a fiber orientation state experimentally determined for long fiber reinforced thermoplastics⁸¹ manufactured by the LFT-D process.⁸² For every combination of fiber volume fraction, fiber orientation tensor and procedure, we generate ten microstructures. The measured runtimes are visualized in Figure 6.

For all fiber orientation tensors, we observe an increase in effort for packings with higher fiber volume fractions. Also, the considered fiber orientation tensor has an influence on the microstructure generation. According to the study, the easiest fiber orientation tensor to realize is the isotropic case and generating the almost planar isotropic case is the hardest. For example, for the fSAM algorithm and the highest volume fraction it takes on average about 5 s to generate the isotropic microstructure but 156 s for the almost planar one. Composites with fiber lengths exceeding the geometry thickness, for example, industrial long fiber reinforced thermoplastics, feature an almost planar fiber arrangement.^{26–29} Comparing the two algorithms for the almost planar fiber orientation states \mathbf{A}_2 – \mathbf{A}_4 , it turns out that the microstructure

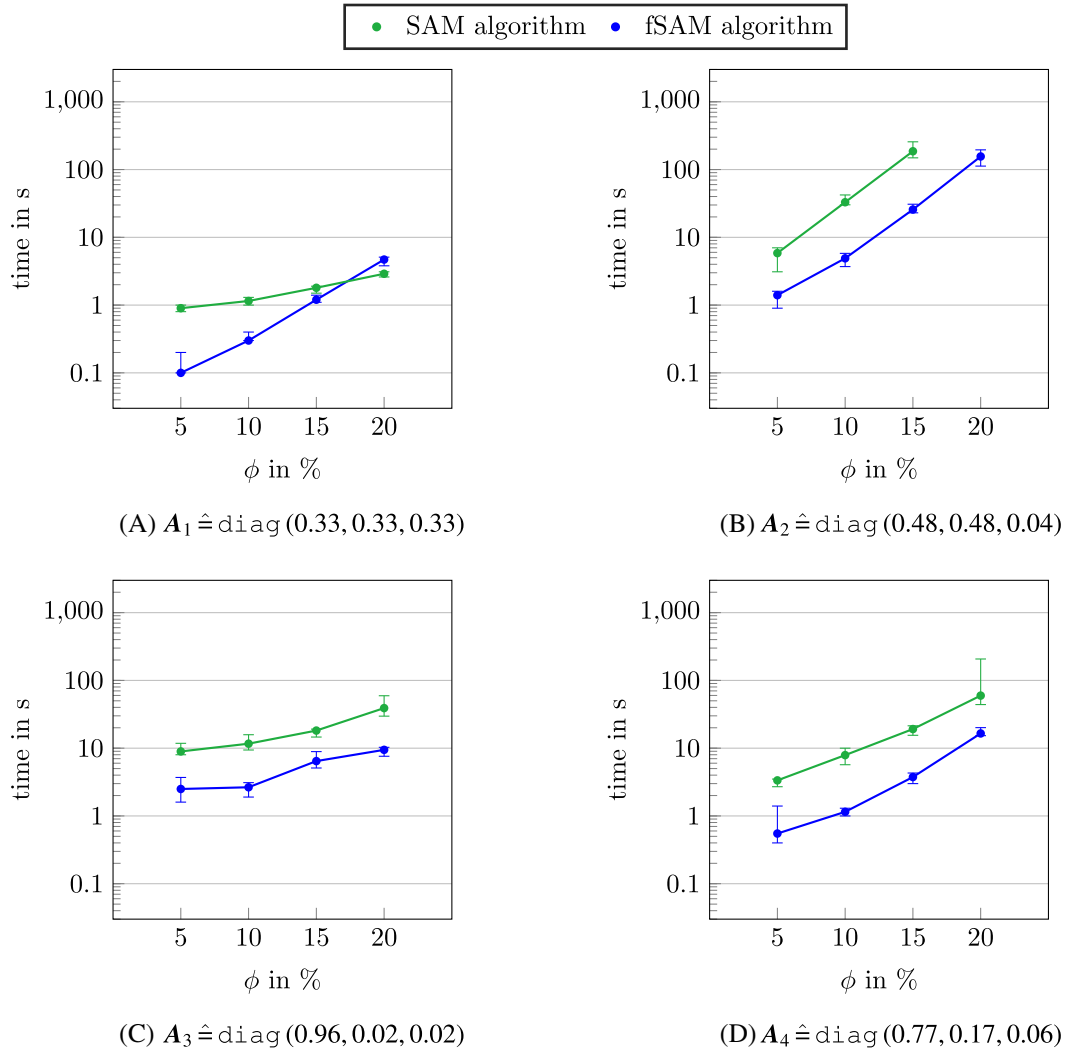


FIGURE 6 Comparison of the runtimes for generating microstructures with four different fiber orientation tensors and fiber volume fractions using the SAM algorithm or the fSAM algorithm.

generation with the fSAM algorithm is always faster than using the SAM algorithm. Especially for the highest volume fraction of 20%, tremendous differences in the runtime are measured. Only for a configuration with an isotropic fiber orientation state and a fiber volume fraction of $\phi = 20\%$, the SAM algorithm is slightly faster than the fSAM algorithm. However, this configuration is not representative for typical LFTs.

Let us focus on the almost planar isotropic case shown in Figure 6B to investigate the differences between the two strategies more thoroughly. For the fiber volume fractions 5%, 10% and 15%, the fSAM algorithm is 4.2, 6.7, and 7.2 times faster than the SAM algorithm. For the highest fiber volume content of 20%, the SAM algorithm fails to converge at all, but the fSAM algorithm is able to generate this microstructure in a mean runtime of 156 s. As filler fractions between 20% and 30% are of primary industrial relevance, the SAM algorithm turns out to be incapable of generating the necessary microstructures, whereas the fSAM algorithm reaches this range. The capability of the fSAM algorithm for even higher fiber volume fractions up to 32% and aspect ratios of 150 is shown in Section 4.6.

Due to the numerical integration of the constrained mechanical system, a single optimization step for the fused fiber procedure takes more time than for the SAM algorithm. Still, the fSAM algorithm turns out to be faster overall, which is a result of the significantly lower number of iteration until convergence. Especially, for complex microstructures, for example, with long fibers or high volume fraction, the SAM algorithm suffers from convergence problems due to the penalty term for the coherence condition. Moving the fibers in a physically meaningful way appears to stabilize the convergence behavior of the optimization algorithm. Hence, we conclude that the adaption of the SAM algorithm with respect to the fSAM algorithm improves the microstructure generation for long fibers immensely. Last but not least, we remark that further reduction in runtime may be achieved by a faster implementation of the numerical integration, for example, with respect to special strategies for the matrix multiplications or the solution of the linear systems of equations.

4.3 | Resolution study

When computing effective properties with computational homogenization techniques, the mesh size needs to be chosen fine enough such that an accurate computation of the properties is enabled.^{77,83} For this purpose, we study the influence of the resolution on the effective stiffness with the reference setup from Section 4.1 and material parameters listed in Table 1. We generate microstructures with a cubic cell-size and cell dimension $Q_i = 612 \mu\text{m}$, which turns out to be large enough for representativity in the RVE study in Section 4.4. The microstructures are filled with a fiber volume fraction of $\phi = 15\%$. A uniform fiber length of $L = 2550 \mu\text{m}$ is considered, that is, an aspect ratio of $r_a = 150$. Due to the maximum segment length of $\bar{\ell} = 100 \mu\text{m}$, the chains consist of 26 segments. We prescribe the fiber orientation tensor of second order $\mathbf{A} \hat{=} \text{diag}(0.77, 0.17, 0.06)$, already used in Section 4.2.

For the resolution, we consider four voxel edge-lengths 6.8, 3.4, 2.0 and $1.7 \mu\text{m}$. Hence, 2.5 voxels resolve a diameter for the coarsest mesh size, whereas 10 voxels resolve a diameter for the finest mesh size. With respect to the total voxel number per microstructure, this results in 90^3 , that is, more than $72 \cdot 10^4$, voxels for the coarsest mesh size and 360^3 , that is, more than $46 \cdot 10^6$, voxels for the finest mesh size. As the effort for the computational homogenization increases with the total voxel number, the homogenization is significantly more time-consuming for the finest mesh size than for the coarsest mesh size. Comparing the voxel edge-lengths to the minimum segment distance of $3.4 \mu\text{m}$, it turns out that the two finest mesh sizes resolve the minimum segment distance with more than one voxel, whereas the voxel edge-length $h = 3.4 \mu\text{m}$ equals the minimum segment distance and the coarsest resolution is not sufficient to resolve the minimum segment distance. In Figure 7, the same microstructure resolved with different voxel edge-lengths are shown. We observe that the fiber directions show a preference in \mathbf{e}_1 -direction and are mainly planar, according to the prescribed fiber orientation tensor of second order.

Let us discuss the computed orthotropic engineering constants, see Table 2. As we approximate the engineering constants from the full effective elastic tensor, we report on the approximation error err_{orth} to control the quality of the approximation. We observe that the approximation error is 2.35% for the coarsest resolution and decreases below 1% for the three other meshes. Hence, in all cases the approximation is adequate to represent the effective stiffness. For the Young's moduli, it turns out that the Young's modulus in \mathbf{e}_1 -direction exceeds the moduli in the other directions by about a factor of three due to the preferred fiber arrangement in \mathbf{e}_1 -direction. As the fibers are rather positioned in \mathbf{e}_2 -direction than in \mathbf{e}_3 -direction, the smallest Young's modulus is E_3 . Also the shear moduli are notably affected by the anisotropic fiber arrangement. According to the order of the fiber orientation tensor components ($a_1 > a_2 > a_3$), the shear moduli decrease from G_{12} to G_{13} to G_{23} . To assess the error induced by the chosen resolution, we compare the moduli with respect

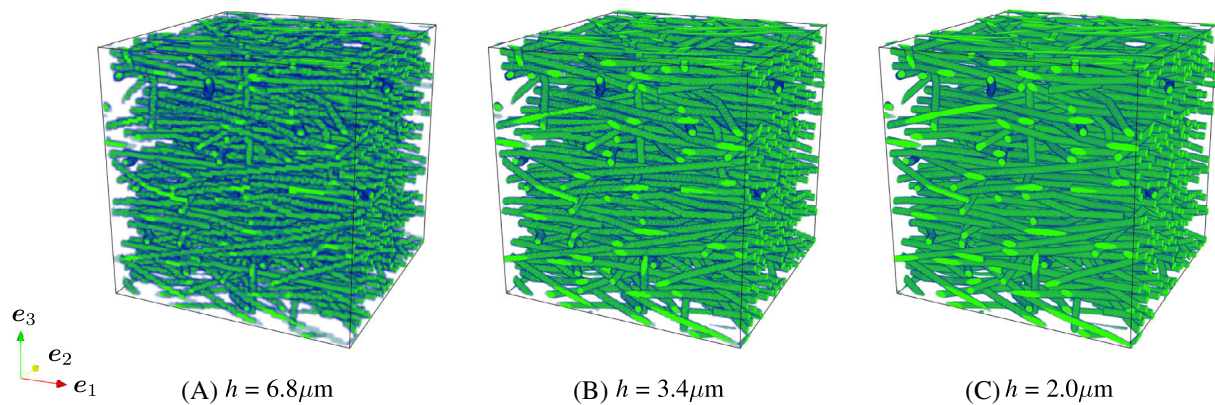


FIGURE 7 Visualization of $(612 \mu\text{m})^3$ -microstructures resolved with three different voxel edge-lengths h .

TABLE 2 Approximated orthotropic engineering constants for the voxel edge-lengths $h = 6.8 \mu\text{m}$, $h = 3.4 \mu\text{m}$, $h = 2.0 \mu\text{m}$, and $h = 1.7 \mu\text{m}$.

h μm	E_1 GPa	E_2 GPa	E_3 GPa	G_{23} GPa	G_{13} GPa	G_{12} GPa	err_{orth} %
6.8	6.10	2.26	2.06	0.75	0.86	1.09	2.35
3.4	6.82	2.32	2.04	0.74	0.85	1.15	0.96
2.0	7.06	2.35	2.03	0.73	0.85	1.17	0.52
1.7	7.11	2.35	2.03	0.73	0.85	1.17	0.44

to the finest mesh. The highest error is computed for the Young's modulus E_1 and the coarsest resolution with 14.21%, dropping to 4.08% and 0.70% for the finer resolutions.

To obtain an error below 3%, we choose a voxel edge-length of $h = 2.0 \mu\text{m}$, that is, 8.5 voxels per diameter. Compared to previous studies for straight^{22,24,84} and curved³¹ fibers with aspect ratios up to 30, where a resolution of 5 voxels per diameter turns out to be sufficient, we observe a higher required resolution for an aspect ratio of 150.

4.4 | On the size of the representative volume element (RVE)

A key concept for computational homogenization of materials with random microstructures is the representativity of unit cells. Due to the randomness of the microstructures, the computed apparent elastic properties on cells of finite volume are *random* variables. Only when assuming infinite cell sizes, the apparent properties become *deterministic* descriptors, known as effective properties. For increasing cell sizes, the apparent properties converge to the effective properties.^{10,85,86} In this context, a unit cell is called representative volume element (RVE) if the computed properties are sufficiently close to the effective properties, that is, the infinite-volume limit of the apparent properties. The computational effort for the homogenization increases with the unit-cell size. Hence, reducing the necessary RVE size is an important factor to ensure time efficient homogenization.

In general, the effective properties are unknown quantities. Hence, it is not possible to compare the apparent properties directly to these quantities. However, the representativity of a unit cell may be assessed without knowing the effective properties in advance. Instead, it is sufficient to monitor two kinds of representativity errors. For a fixed unit-cell size, the *random* error^{10,87} is quantified by the standard deviation of the apparent properties and measures the differences between the realizations. Increasing the unit-cell size reduces the random error.^{32,88} Besides the random error, the mean of the apparent properties may differ from the effective properties, which is called *systematic* error.^{10,87} To monitor the systematic error, we compare the mean of the apparent properties for increasing unit-cell sizes until the mean value converges.

For the RVE study, the setup from Section 4.3 is considered, where the microstructures are resolved with 8.5 voxels per diameter. We study the representativity of three different cubic cell-sizes with dimensions $Q_i = 476 \mu\text{m}$, $Q_i = 612 \mu\text{m}$ and $Q_i = 748 \mu\text{m}$. Hence, the fibers with length $2550 \mu\text{m}$ are several times longer than the cell edge-length, for example, for the smallest cell by about a factor of 5. With respect to the voxel edge-length of $h = 2 \mu\text{m}$, the smallest cell is resolved with 238^3 , that is, more than $13 \cdot 10^6$, voxels and the largest cell with 374^3 , that is, more than $52 \cdot 10^6$, voxels. In Figure 8, generated microstructures for all three cell sizes are shown.

For each cell size, we compute the mean and the standard deviation of the approximated engineering constants for ten realized microstructures. The results are listed in Table 3.

Monitoring the orthotropic approximation error shows that the approximation is suitable with an error below 1% for all three cases. Also for the representativity errors, we observe small deviations, only affecting the second digit. The highest systematic error occurs for the shear modulus G_{12} with a relative error of 0.51%.

It turns out that even the smallest cell size is representative and thus the RVE sizes are small enough to ensure computationally reasonable effort for the homogenization in industrial applications. A further reduction of the cell size is difficult, especially as the smallest cell size only includes 27 fibers and a minimum amount of fibers is necessary to ensure that the microstructure statistics are realized. Additionally, the microstructure generation process is made more challenging as the fibers wrap around the cell even more often. In accordance with previous studies,^{22,31} we emphasize that the combination of periodic boundary conditions and an accurate realization of the prescribed descriptors, for example, as the fourth-order fiber orientation tensor \mathbb{A} , lead to extremely small RVE sizes.

4.5 | Study on the maximum segment length

In this section, we study the influence of the maximum segment length $\bar{\ell}$ on the runtime for the microstructure generation as well as on the computed effective stiffness. Therefore, we consider the setup from Section 4.3 with an edge-length of $Q_i = 612 \mu\text{m}$. The selection of the maximum segment length influences the runtime of the microstructure generation

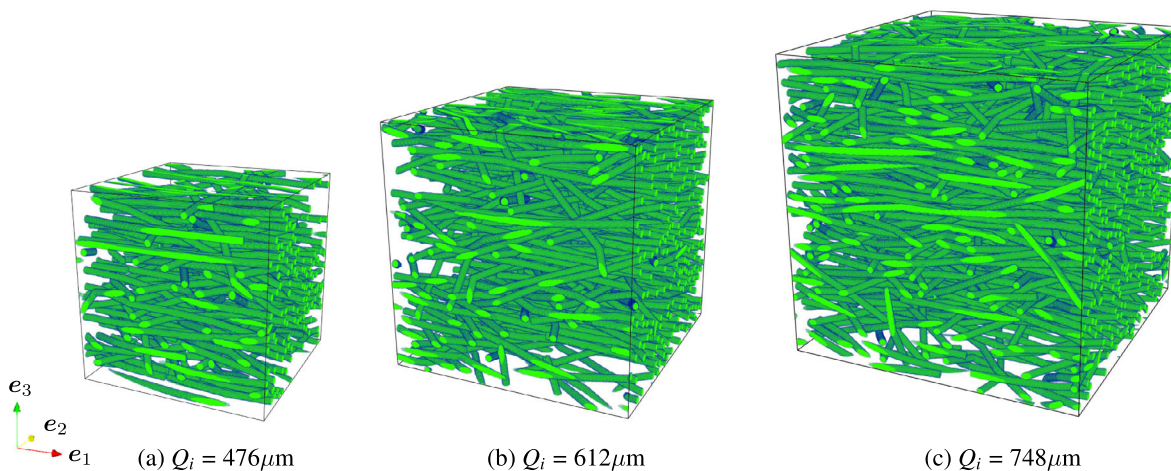


FIGURE 8 Generated microstructures for three different cubic cell-sizes Q_i .

TABLE 3 Approximated orthotropic engineering constants for the cubic cell-sizes $Q_i = 476 \mu\text{m}$, $Q_i = 612 \mu\text{m}$, and $Q_i = 748 \mu\text{m}$.

Q_i μm	E_1 GPa	E_2 GPa	E_3 GPa	G_{23} GPa	G_{13} GPa	G_{12} GPa	err_{orth} %
476	7.09 ± 0.05	2.36 ± 0.02	2.03 ± 0.01	0.73 ± 0.00	0.84 ± 0.01	1.17 ± 0.01	0.55 ± 0.09
612	7.06 ± 0.03	2.35 ± 0.01	2.03 ± 0.00	0.73 ± 0.00	0.84 ± 0.00	1.16 ± 0.01	0.55 ± 0.06
748	7.06 ± 0.02	2.35 ± 0.01	2.03 ± 0.00	0.73 ± 0.00	0.84 ± 0.00	1.17 ± 0.01	0.54 ± 0.03

significantly. To identify an adequate range for the parameter, we study the runtime for varying maximum segment lengths. The considered maximum segment lengths $\bar{\ell}$ and the resulting numbers of segments n are listed in Table 4 with blue color. For all cases, the averaged runtimes of ten microstructure generations are illustrated in Figure 9A by the blue graph.

For the mean runtime, we observe a convex shape with a minimum of 5 s for a maximum segment length of $\bar{\ell} = 100 \mu\text{m}$, that is, the case where the fibers consist of 26 segments. For higher maximum segment lengths, the runtime is increasing and for $\bar{\ell} = 225 \mu\text{m}$, the mean runtime is more than 100s. On the other hand, the microstructure generation is also more expensive for maximum segment lengths smaller than $\bar{\ell} = 100 \mu\text{m}$. Between a maximum segment length of 100 and 52 μm , the gradient is rather small. In contrast, the graph shows an extreme raise for the runtime between 53 μm , that is, 49 segments, and 52 μm , that is, 50 segments. The highest mean runtime is measured for 52 μm of more than 600s.

With increasing maximum segment length, fewer but longer segments are considered. Hence, the possibility of the fibers to fill small free spaces within in the unit cell is hindered, which causes an increase in runtime. Especially, for small RVE sizes the maximum segment length needs to be small as fibers wrapping around a unit cell multiple times harden the microstructure generation and more flexibility is necessary. However, for decreasing maximum segment lengths the increasing number of segments leads to more effort for the numerical integration of the constrained mechanical system and the collision checks. Comparing the latter two tasks, the numerical integration of the constrained mechanical system is the main reason for the increase in runtime. For our investigation, the microstructure generation becomes inefficient whenever certain thresholds are exceeded, for example, the maximum segment length may not be smaller than 53 μm and not larger than 175 μm . For this setup, the maximum segment length $\bar{\ell} = 100 \mu\text{m}$ is identified as best selection with respect to the runtime. The thresholds and the ideal parameter selection depend on the considered setup.

We aim to study the runtimes for the microstructure generation with even smaller maximum segment lengths. To reduce the effort for the numerical integration due to the high number of segments, we use the mixed procedure, see

TABLE 4 Considered maximum segment lengths $\bar{\ell}$ and the resulting numbers of segments n .

$\bar{\ell}$	21	25	50	52	53	75	100	125	150	175	200	225
n	122	102	51	50	49	34	26	21	17	15	13	12

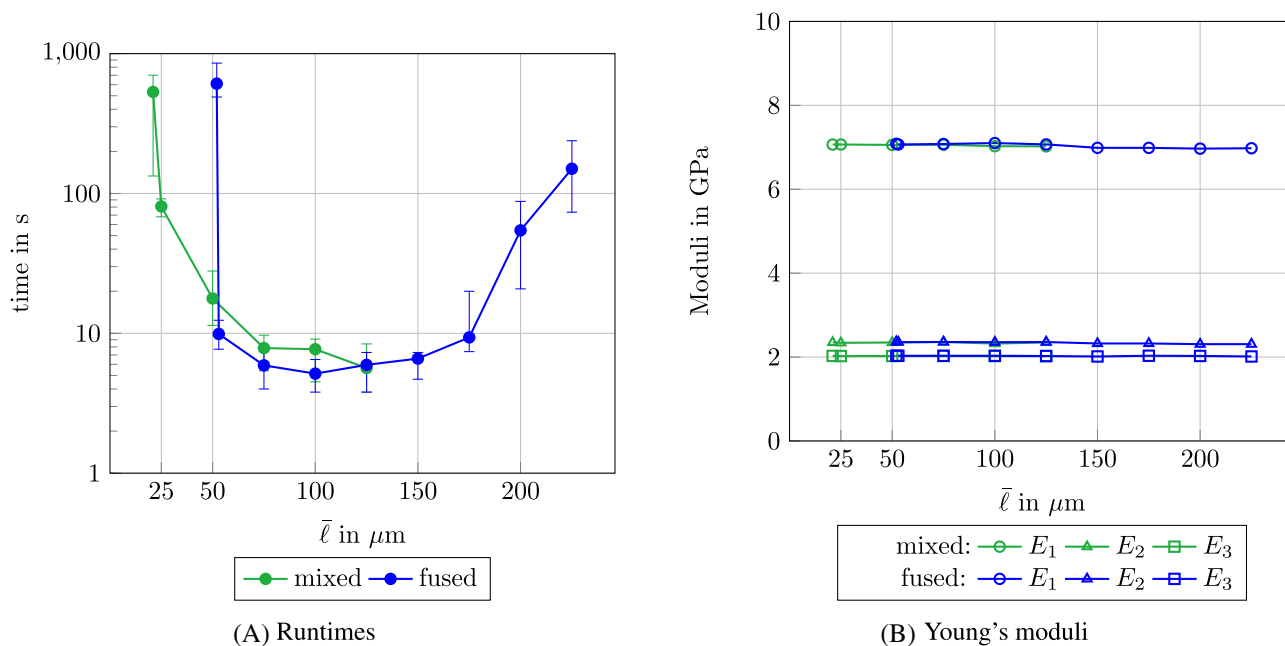


FIGURE 9 Comparison of the runtimes for the microstructure generation (A) and the Young's moduli (B) in terms of different maximum segment lengths $\bar{\ell}$.

Section 3.4. For the study, we consider a maximum number of segments $\bar{n} = 20$ and the segment lengths listed in Table 4 with green text color or boxed. Higher maximum segment lengths than $\bar{\ell} = 125 \mu\text{m}$ are not considered as the resulting segment numbers are smaller than the maximum number of segments $\bar{n} = 20$. Thus, the fibers are discretized with only one chain and the mixed procedure coincides with the pure fSAM algorithm. The measured runtimes are shown by the green graph in Figure 9A.

We observe that the runtimes for the mixed procedure are always higher than for the maximum segment length $\bar{\ell} = 100 \mu\text{m}$ with the fSAM algorithm. Hence, this is still the best parameter and procedure selection for our use case. Considering maximum segment lengths smaller than $\bar{\ell} = 53 \mu\text{m}$, where the fibers are discretized with high numbers of segments, the mixed procedure immensely reduces the runtimes. For example, we observe a runtime of 17.8 s for the maximum segment length $\bar{\ell} = 50 \mu\text{m}$, which is more than 30 times smaller than the runtime for the maximum segment length $\bar{\ell} = 52 \mu\text{m}$ using the fSAM algorithm. However, the green graph shows a significant increase in runtime for maximum segment lengths smaller than $\bar{\ell} = 50 \mu\text{m}$ as the higher number of chains per fiber results in more violation of the coherence condition. For the smallest considered maximum segment length $\bar{\ell} = 21 \mu\text{m}$, a runtime of 533 s is needed. A further reduction of the maximum segment length to $\bar{\ell} = 20 \mu\text{m}$ is not possible as the segment aspect ratio is only slightly higher than one, but the algorithm requires a pronounced spherocylindrical, and not a spherical, segment shape. To conclude, it turns out that the mixed procedure enables microstructure generation for high numbers of segments. However, for moderate number of segments, still the lowest runtime is measured for the fSAM algorithm. Hence, we emphasize that the mixed procedure should only be used to handle extremely long fibers, for example, due to sampling from fiber length distributions.

After studying the influence of the maximum segment length on the runtime of the microstructure generation, we turn our attention to the computed effective stiffnesses. Therefore, we generate microstructures with the maximum segment lengths listed in Table 4, using the fSAM algorithm for the blue written maximum segment lengths and the mixed procedure for the green written or boxed ones. Following Section 4.3, the generated microstructures are resolved with a voxel edge-length of $h = 2.0 \mu\text{m}$. With this setup, the unit cell is representative and the orthotropic approximation is adequate, according to Section 4.4. Hence, we generate only one unit cell for each case to compute the approximated orthotropic effective stiffnesses. The Young's moduli are shown in Figure 9B.

The results show that the stiffness of the microstructures is close for all maximum segment lengths. When comparing the differences with the representativity errors, it even turns out that they are in a similar range. This observation corresponds to a previous study,³¹ investigating the effective properties between curved fibers with a fixed maximum segment length of $\bar{\ell} = 50 \mu\text{m}$, that is, five times the considered diameter of $D = 10 \mu\text{m}$, and straight fibers, that is, the extreme case with a maximum segment length of $\bar{\ell} = \infty$, for different fiber lengths. However, for straight fibers, the microstructure generation and the following homogenization are extremely demanding for high aspect ratios due to the huge necessary unit-cell sizes. Hence, the previous study is restricted to fiber aspect ratios up to $r_a = 90$. By considering rather long maximum segment lengths instead of completely straight fibers, we are capable of confirming the observation of the previous study³¹ also for a significantly higher aspect ratio of $r_a = 150$. Additionally, it turns out that also using maximum segment lengths which are only slightly larger than the diameter does not influence the effective properties remarkably.

4.6 | Generation of microstructures with high fiber volume fractions

We aim to study the limits of the microstructure generation using the fSAM algorithm with respect to a packing with high fiber volume fraction. Therefore, we generate microstructures with a cubic cell-size and cell dimension $Q_i = 612 \mu\text{m}$, a constant fiber length of $L = 2550 \mu\text{m}$ and a fiber orientation tensor of second order $\mathbf{A} \hat{=} \text{diag}(0.77, 0.17, 0.06)$. To pack structures with industrial fiber volume fractions, a high flexibility for the fibers, that is, a small maximum segment length, is required. Hence, we use the maximum segment length $\bar{\ell} = 53 \mu\text{m}$, which is the threshold for an efficient numerical integration of the constrained mechanical system according to Section 4.5. Compared to the fiber diameter $D = 17 \mu\text{m}$, the segments have an aspect ratio of about 3. To study the efficiency of the algorithm with increasing fiber volume fraction, we generate microstructures starting from 20% in 1% steps up to the fiber volume fraction where the algorithm fails to converge within 10^6 iterations.

In Figure 10, the mean and the standard deviation of the runtimes for the microstructure generation are shown, considering ten realizations for each fiber volume fraction. We observe an exponential growth in time for increasing fiber volume fractions. Hence, the smallest runtime is measured for the lowest fiber volume fraction with 21 s. The limit for the fiber volume fraction is reached for $\phi = 32\%$. Notice that the minimum distance between the fibers of $3.4 \mu\text{m}$, that

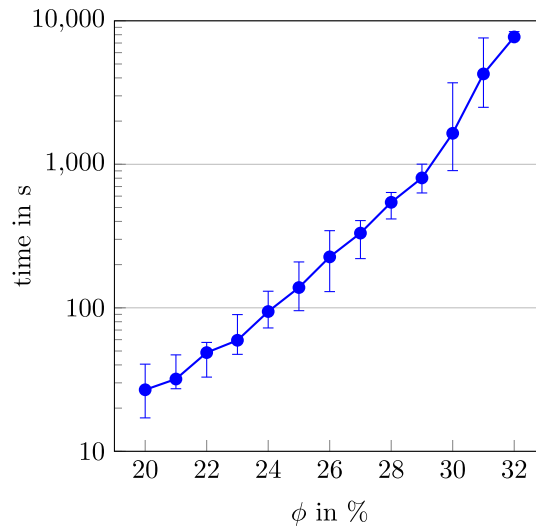


FIGURE 10 Runtimes for the microstructure generation with increasing fiber volume fractions ϕ .

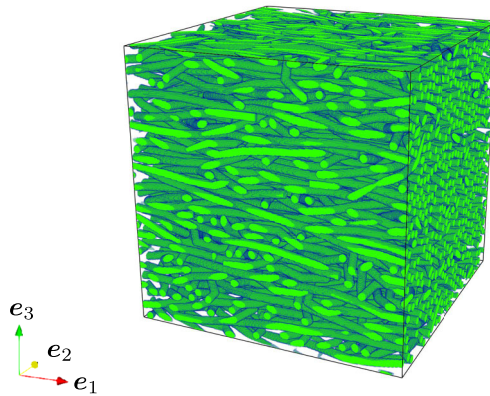


FIGURE 11 Microstructure with aspect ratio $r_a = 150$ and fiber volume fraction $\phi = 32\%$.

is, 20% of the fiber diameter $D = 17 \mu\text{m}$, is realized by increasing the diameter of a fiber during the collision checks by 20%. Hence, the minimum distance increases the fiber volume fraction artificially, and without the minimum distance significantly higher fiber volume fractions may be achievable. A microstructure reinforced with $\phi = 32\%$ fiber volume content is shown in Figure 11. For this case, the runtime is about 7900 s, that is, 2 h 12 min, which is still a low runtime for a packing with such a high fiber volume fraction generated on an ordinary desktop computer. Typically, long fiber reinforced composites are manufactured up to a fiber volume fraction of 30%.^{30,34} Hence, the study shows the capability of the fSAM algorithm to generate microstructure for industrially used LFTs.

4.7 | Application to a PPGF30 material accounting for the fiber length distribution

In this section, we apply the fSAM algorithm, see Sections 3.2 and 3.4, to a PPGF30 material with a fiber volume fraction of $\phi = 13.22\%$ and a second-order fiber orientation tensor $\mathbf{A} \hat{=} \text{diag}(0.71, 0.26, 0.03)$.³⁰ We model the fiber length distribution given by Fliegner et al.³⁰ with a Gamma distribution using a volume-weighted mean of $m = 15.00 \text{ mm}$ and a standard deviation of $s = 14.98 \text{ mm}$. The resulting fiber length distribution is shown in Figure 4. For the microstructure generation, we consider a rectangular unit cell $Q = [0, 1500 \mu\text{m}] \times [0, 1500 \mu\text{m}] \times [0, 750 \mu\text{m}]$. To ensure an efficient numerical integration of the constrained mechanical systems, we use the mixed procedure with a maximum segment

number of $\bar{n} = 20$ and a maximum segment length of $\bar{\ell} = 100$. In Figure 12, a generated microstructure is shown. Due to the fiber length distribution, extremely long fibers are realized. For the visualized microstructure, we highlight the longest fiber, which has a length of $L \approx 48\,976 \mu\text{m}$, in blue and observe that the fiber wraps around the unit cell multiple times. Also, the oscillation of the fibers is apparent.

We aim to realize the volume-weighted mean m and the standard deviation s of the fiber length distribution accurately due to their influence on the effective elastic properties.²⁵ With increasing standard deviation, a higher number of realizations is necessary to obtain adequate statistic quantities. However, when generating microstructures, a large number of fibers results in larger volume element sizes and thus higher computational effort in terms of to the microstructure generation and the subsequent computational homogenization. To reduce the necessary fiber count, we use an improved sampling strategy with scrambled Sobol sequences^{66,67} instead of, for example, the classical Monte Carlo approach. To assess the quality of the realizations, we compare the mean values of the realized statistic quantities with the desired ones. For the considered ten realizations, we obtain a volume-weighted mean of 14.06 mm, which is 6.27% below the desired value of 15.00 mm. For the standard deviation, the mean value is 12.50 mm, that is, 16.56% below the desired value of 14.98 mm. Hence, the volume-weighted mean is realized quite accurately, whereas we observe significantly higher differences for the standard deviation, which is typical for sampling from distribution functions with high standard deviations.

We wish to compare the stiffness of the generated microstructures with experimental data³⁰ and with microstructures generated with the SAM algorithm.³¹ Notice that the latter microstructures include fibers with a constant aspect ratio of $r_a = 240$. For this comparison, we generate ten microstructures, where the mean runtime is about 20 min. Then, we compute the orthotropic Young's moduli with a voxel edge-length of $h = 2.0 \mu\text{m}$, resolving the generated microstructures with $750 \times 750 \times 375$, that is, about 211 million, voxels. Following Schneider,³¹ we use the material parameters $E = 1.8\text{GPa}$ and $\nu = 0.35$ ^{30,35} for the polypropylene matrix. To enable a fair comparison of the runtime with identical hardware, we additionally repeat the study on the SAM algorithm³¹ by generating ten microstructures.

The computed Young's moduli are listed in Table 5, where we add the relative difference with respect to the experimental results in brackets. Comparing the Young's modulus E_1 , the fSAM algorithm shows a good agreement with the experimental results with a relative underestimation of 4.06%, which is closer than the result for the SAM algorithm with 6.47% deviation. The Young's modulus E_2 is overestimated by both procedures slightly with 6.85% for the SAM and 7.49% for the fSAM algorithm. For the Young's modulus E_3 , no experimental results are obtained. However, comparing the two procedures it turns out that the Young's modulus E_3 coincides. Besides the Young's moduli, also the runtimes of the SAM and the fSAM algorithm are listed in Table 5. The mean runtime of the SAM algorithm is about 89 min, which is multiple times higher compared to the fSAM algorithm with 20 min.

Last but not least, we study the highest realizable fiber volume fraction for the considered setup, still using the fiber length distribution shown in Figure 4. Therefore, we increase the fiber volume fraction starting from 15% in 1% steps.

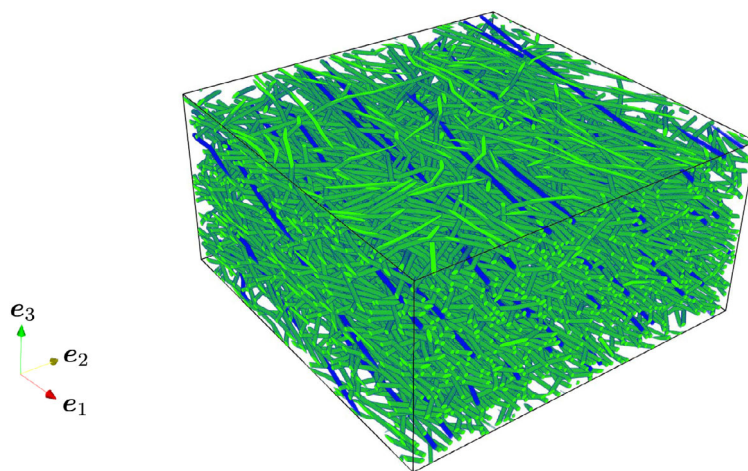


FIGURE 12 Generated microstructure with cell size $Q = [0, 1500 \mu\text{m}] \times [0, 1500 \mu\text{m}] \times [0, 750 \mu\text{m}]$, highlighting the longest fiber with a fiber length of $L \approx 48\,976 \mu\text{m}$.

TABLE 5 Comparison of the experimental results³⁰ and the computed approximated Young's moduli of microstructures generated with the SAM algorithm³¹ or with the fSAM algorithm.

	Experiments ³⁰	SAM algorithm ³¹	fSAM algorithm
E_1 in GPa	6.65	6.22	6.38 ± 0.02
	-	[-6.47%]	[-4.06%]
E_2 in GPa	3.07	3.28	3.30 ± 0.02
	-	[+6.84%]	[+7.49%]
E_3 in GPa	-	2.71	2.71 ± 0.00
Runtime in min	-	88.61 ± 35.72	19.69 ± 4.14

TABLE 6 Runtimes for the microstructure generation of a PPGF material with the fiber length distribution shown in Figure 4 and increasing fiber volume fraction.

ϕ in %	15	16	17	18	19
Runtime in min	34.14 ± 5.81	43.76 ± 4.92	57.61 ± 4.06	87.15 ± 20.95	151.32 ± 23.45

For each fiber volume fraction, we consider five realizations. The runtimes are shown in Table 6. For the highest realizable fiber volume fraction of 19%, the runtime is about 150 min, that is, 2 h30 min.

5 | SUMMARY AND CONCLUSION

This work presents the fused sequential addition and migration (fSAM) algorithm to generate microstructures for composites with long, flexible fibers, which is applicable for industrial fiber aspect ratios and volume fractions. Especially, as the fSAM algorithm generates these microstructures in a computationally efficient manner, the approach represents a promising new tool in the field of reconstruction algorithms for long fiber reinforced composites.

According to the SAM algorithm for long curved fibers,³¹ we model the fibers as polygonal chains with spherocylinders as segments and use an optimization framework for the microstructure generation. As main novelty, we enable a physically meaningful fiber movement within the iterative scheme, where the fibers move in a fused way. However, as a result we optimize on a curved manifold. For this case, the iterates of the basic gradient descent approach may leave the optimization space. To ensure admissible iterates, the gradient steps need to move along the geodesic, that is, the shortest curve between two points on the manifold. In general, such a geodesic is governed by a constrained mechanical system without external forces. Thus, we derive the d'Alembert type constrained mechanical system describing the geodesic of the considered manifold. In a second step, an efficient numerical method for the integration of the constrained mechanical system is presented. Additionally, we discuss the adaption of the SAM algorithm for long curved fibers³¹ to account for the fused fiber movement. For the fiber length distribution, we use the Gamma distribution, which is capable of realizing the main characteristics of the fiber lengths measured for long fiber reinforced microstructures.^{30,34,35} In context of extremely long fibers, we introduce a workaround to overcome the high computational effort due to the numerical integration of the constrained mechanical system.

We briefly summarize the findings of the computational investigations:

- First, a study on the efficiency of the SAM algorithm and the fSAM algorithm is provided, considering constant fiber lengths. The results show that generating microstructures with the fSAM algorithm is multiple times faster than with the SAM algorithm. Whereas the SAM algorithm fails to generate microstructures with a fiber volume fraction of 20%, an aspect ratio of about 90 and an almost planar isotropic fiber orientation state, the fSAM algorithm is capable of generating this microstructure in a routine way. The packing with higher fiber volume fraction is enabled as the fused fiber movement stabilizes the convergence behavior of the optimization algorithm.
- To ensure the representativity of the generated unit cells, even the smallest considered cell size may be used as RVE. In these unit cells only 27 fibers are included. Hence, the fSAM algorithm ensures appropriate cell sizes leading to a reasonable effort for the subsequent computational homogenization.

- A parameter study of the maximum segment length is included in the computational investigations, showing that the selection of the parameter has significant influence on the runtime but almost no effect on the effective properties. On the one hand, the maximum segment length needs to be sufficient small to ensure the necessary flexibility of the fibers. On the other hand, with decreasing maximum segment length more segments are used to discretize the fiber, which leads to an increased effort for the numerical integration of the constrained mechanical system and the collision checks. Hence, for every considered use case an adequate parameter selection is mandatory. Considering the computed effective stiffness for different maximum segment lengths, the deviations are rather small, below 3%.
- To prove the capability of the fSAM algorithm to generate microstructures with industrial fiber volume fraction, a study is included considering constant fiber lengths and an experimentally measured orthotropic fiber orientation tensor of second order $\mathbf{A} \hat{=} \text{diag}(0.77, 0.17, 0.06)$.⁸¹ The highest achieved fiber volume fraction is 32% for a fiber aspect ratio of 150, generated in 2 h 12 min. Hence, also high-performance materials reinforced by high fiber volume fractions are covered by the algorithm. Indeed, for typical standard materials up to a fiber volume fraction of 25% the runtime is within 3 min. Studying the maximum fiber volume fractions for varying fiber orientation states may be part of further investigations.
- The method is capable of generating microstructures for an industrial PPGF30 material with a fiber volume fraction of 13.22%, accounting for its fiber length distribution. Sampling from the Gamma distribution leads to extremely long fibers, for example, in this case up to a length of 49 mm, that is, an aspect ratio of $r_a \approx 2881$. By comparing the computed effective properties to experimental results, the computed Young's modulus E_1 is in good coincidence with experiments, leading to a relative underestimation by 4.06%. The computed Young's modulus E_2 slightly overestimates the experiments with a relative deviation of 7.49%.

To sum up the numerical investigations, considering physically meaningful fiber motion as the key novelty within the fSAM algorithm improves the capability for generating microstructures of composites with long, curved fibers significantly. Thus, on the one hand, higher fiber volume fractions for long fiber reinforced composites are achievable, enabling microstructure generation also for high-performance LFTs with more than 30% fiber volume content. On the other hand, the microstructure generation is more efficient due to the reduced runtimes. Also, with respect to the subsequent numerical homogenization, reasonable computational effort is ensured by small RVE sizes. The methodology demonstrates to be suitable for industrial materials, featuring fiber length distribution with extremely long fibers, when applied to a PPGF30 material. Moreover, comparing the computed effective properties of generated PPGF30 microstructures to experimental data shows good coincidence.

AUTHOR CONTRIBUTIONS

Celine Lauff: conceptualization, methodology, software, validation, formal analysis, investigation, data curation, writing – original draft, writing – review & editing, visualization, project administration. **Matti Schneider:** conceptualization, methodology, formal analysis, resources, writing – review & editing, supervision, project administration, funding acquisition. **John Montesano:** writing – review & editing, supervision. **Thomas Böhlke:** resources, writing – review & editing, supervision, project administration, funding acquisition. All authors read and approved the manuscript.

ACKNOWLEDGMENTS

We thank the anonymous reviewers for their insightful comments and valuable suggestions which led to improvements of the manuscript. The research documented in this manuscript was funded by the German Research Foundation (DFG), project number 255730231, within the International Research Training Group “Integrated engineering of continuous-discontinuous long fiber reinforced polymer structures” (GRK 2078). The support by the German Research Foundation (DFG) is gratefully acknowledged. Support from the European Research Council within the Horizon Europe program–project 101040238–is gratefully acknowledged by Matti Schneider. Open Access funding enabled and organized by Projekt DEAL.

CONFLICT OF INTEREST STATEMENT

The authors declare that they have no conflict of interest.

DATA AVAILABILITY STATEMENT

The data that support the findings of this study is available from the author upon reasonable request.

ORCID

Celine Lauff  <https://orcid.org/0000-0003-4046-171X>

Matti Schneider  <https://orcid.org/0000-0001-7017-3618>

Thomas Böhlke  <https://orcid.org/0000-0001-6884-0530>

REFERENCES

1. dRF P, Bisiaux M, Lynch J, Rosenberg E. High resolution x-ray tomography in an electron microprobe. *Rev Sci Instrum.* 1996;67(6):2251-2256.
2. Shen H, Nutt S, Hull D. Direct observation and measurement of fiber architecture in short fiber-polymer composite foam through micro-CT imaging. *Compos Sci Technol.* 2004;64(13-14):2113-2120.
3. Buck F, Brylka B, Müller V, et al. Two-scale structural mechanical modeling of long fiber reinforced thermoplastics. *Compos Sci Technol.* 2017;117:159-167.
4. Kuhn C, Walter I, Taeger O, Osswald A. Experimental and numerical analysis of fiber matrix separation during compression molding of long fiber reinforced thermoplastics. *J Compos Sci.* 2017;1(1):2.
5. Matouš K, Geers MGD, Kouznetsova VG, Gillman A. A review of predictive nonlinear theories for multiscale modeling of heterogeneous materials. *J Comput Phys.* 2017;330:192-220.
6. Geers MGD, Kouznetsova V, Brekelmans WAM. Multi-scale computational homogenization: trends and challenges. *Mech Mater.* 2010;234(7):2175-2182.
7. Saeb S, Steinmann P, Javili A. Aspects of computational homogenization at finite deformations: a unifying review from Reuss' to Voigt's Bound. *Appl Mech Rev.* 2016;68(5):050801.
8. Otero F, Oller S, Martinez X. Multiscale computational homogenization: review and proposal of a new enhanced-first-order method. *Arch Comput Methods Eng.* 2018;25:479-505.
9. Bargmann S, Klusemann B, Markmann J, et al. Generation of 3D representative volume elements for heterogeneous materials: A review. *Prog Mater Sci.* 2018;96:322-384.
10. Kanit T, Forest S, Galliet I, Mounoury V, Jeulin D. Determination of the size of the representative volume element for random composites: statistical and numerical approach. *Int J Solids Struct.* 2003;40(13-14):3647-3679.
11. Sab K, Nedjar B. Periodization of random media and representative volume element size for linear composites. *Comptes Rendus Mécanique.* 2005;333(2):187-195.
12. Schneider M, Josien M, Otto F. Representative volume elements for matrix-inclusion composites—a computational study on the effects of an improper treatment of particles intersecting the boundary and the benefits of periodizing the ensemble. *J Mech Phys Solids.* 2022;158:104652.
13. Widom B. Random sequential addition of hard spheres to a volume. *J Chem Phys.* 1966;44(10):3888-3894.
14. Feder J. Random sequential adsorption. *J Theor Biol.* 1980;87(2):237-254.
15. Evans KE, Gibson AG. Prediction of the maximum packing fraction achievable in randomly oriented short-fibre composites. *Compos Sci Technol.* 1986;25:149-162.
16. Toll S. Packing mechanics of fiber reinforcements. *Polym Eng Sci.* 1998;38(8):1337-1350.
17. Tian W, Qi L, Zhou J, Ma Y. Representative volume element for composites reinforced by spatially randomly distributed discontinuous fibers and its applications. *Compos Struct.* 2013;131(7):366-373.
18. Chen L, Gu B, Zhou J, Tao J. Study of the effectiveness of the RVEs for random short fiber reinforced elastomer composites. *Fibers Polym.* 2019;20(7):1467-1479.
19. Bahmani A, Li G, Willett TL, Montesano J. Three-dimensional micromechanical assessment of biomimetic composites with non-uniformly dispersed inclusions. *Compos Struct.* 2019;212:484-499.
20. Tian W, Chao X, Fu MW, Qi L. An advanced method for efficiently generating composite RVEs with specified particle orientation. *Compos Sci Technol.* 2021;205:108647.
21. Bahmani A, Nooraie RY, Willett TL, Montesano J. A sequential mobile packing algorithm for micromechanical assessment of heterogeneous materials. *Compos Sci Technol.* 2023;237(2):110008.
22. Lauff C, Schneider M, Montesano J, Böhlke T. An orientation corrected shaking method for the microstructure generation of short fiber-reinforced composites with almost planar fiber orientation. *Compos Struct.* 2023;323:117352.
23. Williams S, Philipse A. Random packings of spheres and spherocylinders simulated by mechanical contraction. *Phys Rev E.* 2003;67(5):1-9.
24. Schneider M. The sequential addition and migration method to generate representative volume elements for the homogenization of short fiber reinforced plastics. *Comput Mech.* 2017;59:247-263.
25. Mehta A, Schneider M. A sequential addition and migration method for generating microstructures of short fibers with prescribed length distribution. *Comput Mech.* 2022;70(4):829-851.
26. Advani SG, Tucker CL III. A numerical simulation of short fiber orientation in compression molding. *Polym Compos.* 1990;11(3):164-173.
27. Dray D, Gilormini P, Régner G. Comparison of several closure approximations for evaluating the thermoelastic properties of an injection molded short-fiber composite. *Compos Sci Technol.* 2007;67(7-8):1601-1610.
28. Bernasconi A, Cosmi F, Hine PJ. Analysis of fibre orientation distribution in short fibre reinforced polymers: A comparison between optical and tomographic methods. *Compos Sci Technol.* 2012;72(16):2002-2008.

29. Görthöfer J, Meyer N, Pallicity TD, et al. Virtual process chain of sheet molding compound: development, validation and perspectives. *Compos Part B*. 2019;169:133-147.
30. Fliegenger S, Luke M, Gumbsch P. 3D microstructure modeling of long fiber reinforced thermoplastics. *Compos Sci Technol*. 2014;104:136-145.
31. Schneider M. An algorithm for generating microstructures of fiber-reinforced composites with long fibers. *Int J Numer Methods Eng*. 2022;123(24):6197-6219.
32. Jeulin D. Power laws variance scaling of boolean random varieties. *Methodol Comput Appl Probab*. 2016;18(4):1065-1079.
33. Willot F. Mean covariogram of cylinders and applications to boolean random sets. *J Contemp Math Anal (Armen Acad Sci)*. 2017;52(6):305-315.
34. Nguyen BN, Bapanapalli SK, Holbery JD, et al. Fiber length and orientation in long-fiber injection-molded thermoplastics — Part I: Modeling of microstructure and elastic properties. *J Compos Mater*. 2008;42(10):1003-1029.
35. Senior AB, Osswald T. Measuring fiber length in the core and shell regions of injection molded long fiber reinforced thermoplastic plaques. *J Composit Sci*. 2020;4(3):104.
36. do Carmo MP. *Riemannian Geometry*. Birkhäuser; 1992.
37. Petersen P. *Riemannian Geometry*. Graduate Texts in Mathematics. Vol 171. Springer; 2016.
38. Angleses J, Lee S. The modelling of holonomic mechanical systems using a natural orthogonal complement. *Trans Can Soc Mech Eng*. 2005;13(4):81-89.
39. Betsch P. The discrete null space method for the energy consistent integration of constrained mechanical systems: Part I: Holonomic constraints. *Comput Methods Appl Mech Eng*. 2005;194(50–52):5159-5190.
40. Garcia AG. *Random Packings via Mechanical Contraction*. Master's thesis, Universiteit Utrecht; 2015.
41. Meyer C. *Matrix Analysis and Applied Linear Algebra Book with Solutions*. Society for Industrial and Applied Mathematics; 2000.
42. Gonzales O. Mechanical systems subject to holonomic constraints: differential-algebraic formulations and conservative integration. *Phys D*. 1999;132(132):165-174.
43. Gonzales O. Time integration and discrete Hamiltonian systems. *J Nonlinear Sci*. 1996;6:449-467.
44. Boyd S, Vandenberghe L. *Convex Optimization*. Cambridge University Press; 2004.
45. Goodman AW, Goodman G. Generalizations of the theorems of pappus. *Am Math Mon*. 1969;76(4):355-366.
46. Kanatani KI. Distribution of directional data and fabric tensors. *Int J Eng Sci*. 1984;22(2):149-164.
47. Advani SG, Tucker CL III. The use of tensors to describe and predict fiber orientation in short fiber composites. *J Rheol*. 1987;31:751-784.
48. Krause M, Hausherr JM, Burgeth B, Herrmann C, Krenkel W. Determination of the fibre orientation in composites using the structure tensor and local X-ray transform. *J Mater Sci*. 2010;45(4):888-896.
49. Wirjadi O, Schladitz K, Easwaran P, Ohser J. Estimating fibre direction distributions of reinforced composites from tomographic images. *Image Anal Stereolog*. 2016;35(3):167-179.
50. Hessman PA, Riedel T, Welschinger F, Hornberger K, Böhlke T. Microstructural analysis of short glass fiber reinforced thermoplastics based on x-ray micro-computed tomography. *Compos Sci Technol*. 2019;183:107752.
51. Müller V, Böhlke T. Prediction of effective elastic properties of fiber reinforced composites using fiber orientation tensors. *Compos Sci Technol*. 2016;130:36-45.
52. Bauer JK, Böhlke T. On the dependence of orientation averaging mean field homogenization on planar fourth-order fiber orientation tensors. *Mech Mater*. 2022;170:104307.
53. Folgar F, Tucker CL III. Orientation behaviour of fibers in concentrated suspensions. *J Reinf Plast Compos*. 1984;3:98-119.
54. Cintra JS, Tucker CL III. Orthotropic closure approximations for flow-induced fiber orientation. *J Rheol*. 1995;39(6):1095-1122.
55. Breuer K, Stommel M, Korte W. Analysis and evaluation of fiber orientation reconstruction methods. *J Compos Sci*. 2019;3(3):67.
56. Kugler SK, Kech A, Cruz C, Osswald T. Fiber orientation predictions—A review of existing models. *J Compos Sci*. 2020;4(2):69.
57. Karl T, Gatti D, Frohnafel B, Böhlke T. Asymptotic fiber orientation states of the quadratically closed Folgar-Tucker equation and a subsequent closure improvement. *J Rheol*. 2021;65(5):999-1022.
58. Karl T, Schneider M, Böhlke T. On fully symmetric implicit closure approximations for fiber orientation tensors. *J Non-Newtonian Fluid Mech*. 2023;318:105049.
59. Montgomery-Smith S, He W, Jack D, Smith DE. Exact tensor closures for the three-dimensional Jeffery's equation. *J Fluid Mech*. 2011;680:321-335.
60. Montgomery-Smith S, Jack D, Smith DE. The Fast Exact Closure for Jeffery's equation with diffusion. *J Non-Newtonian Fluid Mech*. 2011;166:343-353.
61. Vega C, Lago S. A fast algorithm to evaluate the shortest distance between rods. *Comput Chem*. 1994;67–68:56-70.
62. Pournin I, Weber M, Tsukahara M, Ferrez JA, Ramaioli M, Liebling TM. Three-dimensional distinct element simulation of spherocylinder crystallization. *Granul Matter*. 2005;7:119-126.
63. Allen MP, Tildesley DJ. *Computer Simulation of Liquids*. Clarendon Press; 1987.
64. Verlet L. Computer 'experiments' on classical fluids. I. Thermodynamical properties of Lennard-Jonear molecules. *Phys Rev*. 1967;159:98-103.
65. Papoulis AP, Unnikrishna PS. *Probability, Random Variables, and Stochastic Processes*. 4th ed. McGraw-Hill; 2002.
66. Sobol IM. On the distribution of points in a cube and the approximate evaluation of integrals. *USSR Comput Math Math Phys*. 1967;7(4):86-112.
67. Sobol IM. Uniformly distributed sequences with additional uniformity properties. *USSR Comput Math Math Phys*. 1967;16(5):236-242.

68. Hammersley JM, Handscomb DC. *Monte Carlo Methods*. Chapman and Hall; 1964.
69. DOW® Chemical Company. *C711–70RNA polypropylene resin*. Product information; 2003.
70. PPG Fiber Glass. TufRov® 4575. Data Sheet 2013.
71. Böhm HJ, Eckschlager A, Han W. Multi-inclusion unit cell models for metal matrix composites with randomly oriented discontinuous reinforcements. *Comput Mater Sci*. 2002;25(1–2):42–53.
72. Pan Y, Pelegri AA, Iorga L. Analysis of 3D random chopped fiber reinforced composite using the finite element method. *Comput Mater Sci*. 2008;43(3):450–461.
73. Moulinec H, Suquet P. A fast numerical method for computing the linear and nonlinear mechanical properties of composites. *Comptes Rendus de l'Académie des Sciences Série II*. 1994;318(11):1417–1423.
74. Moulinec H, Suquet P. A numerical method for computing the overall response of nonlinear composites with complex microstructure. *Comput Methods Appl Mech Eng*. 1998;157:69–94.
75. Schneider M, Ospald F, Kabel M. Computational homogenization of elasticity in a staggered grid. *Int J Numer Methods Eng*. 2016;105(9):693–720.
76. Zeman J, Vondřejc J, Novak J, Marek I. Accelerating a FFT-based solver for numerical homogenization of periodic media by conjugate gradients. *J Comput Phys*. 2010;229(21):8065–8071.
77. Brisard S, Dormieux L. Combining Galerkin approximation techniques with the principle of Hashin and Shtrikman to derive a new FFT-based numerical method for the homogenization of composites. *Comput Methods Appl Mech Eng*. 2012;217–220:197–212.
78. Cowin SC. The relationship between the elasticity tensor and the fabric tensor. *Mech Mater*. 1985;4(2):137–147.
79. Bauer JK, Böhlke T. Variety of fiber orientation tensors. *Math Mech Solids*. 2022;27(7):1185–1211.
80. Görthöfer J, Schneider M, Ospald F, Hrymak A, Böhlke T. Computational homogenization of sheet molding compound composites based on high fidelity representative volume elements. *Comput Mater Sci*. 2020;174:109456.
81. Blarr J, Sabiston T, Krauß C, et al. Implementation and comparison of algebraic and machine learning based tensor interpolation methods applied to fiber orientation tensor fields obtained from CT images. *Comput Mater Sci*. 2023;228:112286.
82. Krause W, Henning F, Tröster S, Geiger O, Eyerer P. LFT-D—A process technology for large scale production of fiber reinforced thermoplastic components. *J Thermoplast Compos Mater*. 2003;289–302(4):117352.
83. Schneider M. Convergence of FFT-based homogenization for strongly heterogeneous media. *Math Methods Appl Sci*. 2015;38(13):2761–2778.
84. Müller V, Kabel M, Andrä H, Böhlke T. Homogenization of linear elastic properties of short-fiber reinforced composites—A comparison of mean field and voxel-based methods. *Int J Solids Struct*. 2015;67–68:56–70.
85. Hill R. Elastic properties of reinforced solids: Some theoretical principles. *J Mech Phys Solids*. 1963;11(5):357–372.
86. Drugan WJ, Willis JR. A micromechanics-based nonlocal constitutive equations and estimates of representative volume element size for elastic composites. *J Mech Phys Solids*. 1996;44:497–524.
87. Gloria A, Otto F. An optimal variance estimate in stochastic homogenization of discrete elliptic equations. *Ann Probab*. 2011;39(3):779–856.
88. Dirrenberger J, Forest S, Jeulin D. Towards gigantic RVE sizes for 3D stochastic fibrous networks. *Int J Solids Struct*. 2014;51(2):359–376.
89. Hand IN, Finch JD. *Analytical Mechanics*. fourth ed. Cambridge University Press; 1998.

How to cite this article: Lauff C, Schneider M, Montesano J, Böhlke T. Generating microstructures of long fiber reinforced composites by the fused sequential addition and migration method. *Int J Numer Methods Eng*. 2024;e7573. doi: 10.1002/nme.7573

APPENDIX A. METRIC OF THE RIEMANNIAN MANIFOLD DESCRIBING A CURVED FIBER

The purpose of this appendix is to provide a streamlined derivation of the natural metric g of the manifold \mathcal{R} (20), that is, Equation (24). The manifold \mathcal{R} parametrizes the submanifold \mathcal{F} (14) of the Euclidean space \mathbb{R}^{6n} , whose general elements we will denote as \mathbf{f} . More precisely, the coordinate vector \mathbf{f} collects the midpoints \mathbf{x}^a and the directions \mathbf{p}^a of all segments, see Equation (13). For the Euclidean space at $\mathbf{f} \in \mathbb{R}^{6n}$, the scalar product of a tangent vector $\dot{\mathbf{f}} \in T_{\mathbf{f}}\mathbb{R}^{6n} \equiv \mathbb{R}^{6n}$ computes as

$$\langle \dot{\mathbf{f}}, \dot{\mathbf{f}} \rangle_{\mathbb{R}^{6n}} = \sum_{a=1}^n \left[\|\dot{\mathbf{x}}^a\|^2 + \varepsilon(\ell, D) \|\dot{\mathbf{p}}^a\|^2 \right], \quad (\text{A1})$$

where the volume-specific moment of inertia of a spherocylinder $\varepsilon(\ell, D)$ (25) is responsible for the specific form of the rotational contributions. With the Equation (A1) at hand, the metric g of the manifold \mathcal{R} is obtained via the pull-back (9) of the scalar product in Equation (A1) onto the tangent space $T_{\mathbf{q}}\mathcal{R}$

$$g_{\mathbf{q}}(\dot{\mathbf{q}}, \dot{\mathbf{q}}) = \langle d\mathbf{f}_{\mathbf{q}}(\dot{\mathbf{q}}), d\mathbf{f}_{\mathbf{q}}(\dot{\mathbf{q}}) \rangle_{\mathbb{R}^{6n}}, \quad \mathbf{q} \in \mathcal{R}, \quad \dot{\mathbf{q}} \in T_{\mathbf{q}}\mathcal{R}, \quad (\text{A2})$$

with the explicit formulation for the differential map $d\mathbf{f}_{\mathbf{q}}$

$$d\mathbf{f}_{\mathbf{q}}(\dot{\mathbf{q}}) = \left[(dx_{\mathbf{q}}^1(\dot{\mathbf{q}}))^T \cdots (dx_{\mathbf{q}}^n(\dot{\mathbf{q}}))^T (d\mathbf{p}_{\mathbf{q}}^1(\dot{\mathbf{q}}))^T \cdots (d\mathbf{p}_{\mathbf{q}}^n(\dot{\mathbf{q}}))^T \right]^T, \quad \mathbf{q} \in \mathcal{R}, \quad \dot{\mathbf{q}} \in T_{\mathbf{q}}\mathcal{R} \quad (\text{A3})$$

with $dx_{\mathbf{q}}^a(\dot{\mathbf{q}}) = \hat{\mathbf{Q}} \dot{\mathbf{x}}^0 + \sum_{b=1}^{a-1} \ell \dot{\mathbf{p}}^b + \frac{\ell}{2} \dot{\mathbf{p}}^a$ and $d\mathbf{p}_{\mathbf{q}}^a(\dot{\mathbf{q}}) = \dot{\mathbf{p}}^a$, $a = 1, \dots, n$

from the tangent space $T_{\mathbf{q}}\mathcal{R}$ onto the tangent space $T_{f(\mathbf{q})}\mathcal{F}$. Using the explicit formulation of the differential map $d\mathbf{f}_{\mathbf{q}}$ in Equation (A3) leads to

$$g_{\mathbf{q}}(\dot{\mathbf{q}}, \dot{\mathbf{q}}) = \sum_{a=1}^n \left[\|dx^a(\dot{\mathbf{q}})\|^2 + \varepsilon(\ell, D) \|d\mathbf{p}^a(\dot{\mathbf{q}})\|^2 \right] \quad (\text{A4})$$

$$= \sum_{a=1}^n \left[\left\| \hat{\mathbf{Q}} \dot{\mathbf{x}}^0 + \sum_{b=1}^{a-1} \ell \dot{\mathbf{p}}^b + \frac{\ell}{2} \dot{\mathbf{p}}^a \right\|^2 + \varepsilon(\ell, D) \|\dot{\mathbf{p}}^a\|^2 \right].$$

Equation (A4) reveals that the metric of the manifold \mathcal{R} is independent of the location on the manifold $g_{\mathbf{q}} \equiv g$. We wish to give the metric g in Equation (A4) in the form of

$$g(\dot{\mathbf{q}}, \dot{\mathbf{q}}) = \dot{\mathbf{q}}^T \mathbf{G} \dot{\mathbf{q}}, \quad (\text{A5})$$

with the constant metric matrix \mathbf{G} . As the metric g is already known, the metric matrix \mathbf{G} may be derived by the relation

$$\mathbf{G} = \frac{1}{2} \frac{\partial^2 g}{\partial \dot{\mathbf{q}} \partial \dot{\mathbf{q}}}. \quad (\text{A6})$$

We compute the first derivative of the halved metric with regard to the normalized starting point

$$\frac{1}{2} \frac{\partial g}{\partial \dot{\mathbf{x}}^0} = \sum_{a=1}^n \hat{\mathbf{Q}} \left[\hat{\mathbf{Q}} \dot{\mathbf{x}}^0 + \sum_{b=1}^{a-1} \ell \dot{\mathbf{p}}^b + \frac{\ell}{2} \dot{\mathbf{p}}^a \right] = n \hat{\mathbf{Q}}^2 \dot{\mathbf{x}}^0 + \sum_{a=1}^n \left(n - a + \frac{1}{2} \right) \ell \hat{\mathbf{Q}} \dot{\mathbf{p}}^a \quad (\text{A7})$$

and with regard to the directions

$$\frac{1}{2} \frac{\partial g}{\partial \dot{\mathbf{p}}^a} = \ell \sum_{b=a+1}^n \left(\hat{\mathbf{Q}} \dot{\mathbf{x}}^0 + \sum_{c=1}^{b-1} \ell \dot{\mathbf{p}}^c + \frac{\ell}{2} \dot{\mathbf{p}}^b \right) + \frac{\ell}{2} \left(\hat{\mathbf{Q}} \dot{\mathbf{x}}^0 + \sum_{b=1}^{a-1} \ell \dot{\mathbf{p}}^b + \frac{\ell}{2} \dot{\mathbf{p}}^a \right) + \varepsilon(\ell, D) \dot{\mathbf{p}}^a \quad (\text{A8})$$

$$= \left(n - a + \frac{1}{2} \right) \ell \hat{\mathbf{Q}} \dot{\mathbf{x}}^0 + \sum_{b=1}^{a-1} \left(n - a + \frac{1}{2} \right) \ell^2 \dot{\mathbf{p}}^b + \left(\varepsilon(\ell, D) + \ell^2 \left(n - a + \frac{1}{4} \right) \right) \dot{\mathbf{p}}^a + \sum_{b=a+1}^n \left(n - b + \frac{1}{2} \right) \ell^2 \dot{\mathbf{p}}^b.$$

Hence, the metric matrix attains the form

$$\mathbf{G} = \begin{bmatrix} n \hat{\mathbf{Q}}^2 & f_1 \ell \hat{\mathbf{Q}} & f_2 \ell \hat{\mathbf{Q}} & \cdots & f_n \ell \hat{\mathbf{Q}} \\ & f_{d,1} \mathbf{1}_{3 \times 3} & f_2 \ell^2 \mathbf{1}_{3 \times 3} & \cdots & f_n \ell^2 \mathbf{1}_{3 \times 3} \\ & & \ddots & & \vdots \\ & & & \ddots & f_n \ell^2 \mathbf{1}_{3 \times 3} \\ \text{sym} & & & & f_{d,n} \mathbf{1}_{3 \times 3} \end{bmatrix} \quad \text{with } f_a = n - a + \frac{1}{2} \quad \text{and } f_{d,a} = \varepsilon(\ell, D) + \ell^2 \left(n - a + \frac{1}{4} \right). \quad (\text{A9})$$

where the latter equation corresponds to Equation (24).

APPENDIX B. GEODESICS ON THE RIEMANNIAN MANIFOLD OF CURVED FIBERS

The goal of this appendix is to derive the equations governing the geodesics of the manifold describing curved fibers \mathcal{R} (20). Suppose that we know the coordinate vector at the time points t_1 and t_2 and aim to describe the geodesic curve between these instants. According to Equation (5), the geodesic of the manifold \mathcal{R} may be obtained by minimizing the energy functional, parametrizing the midpoints and directions by the coordinate vector $\mathbf{q}(t) \in \mathbb{R}^{n_q}$, see Equation (18), under the condition that the vector-valued constraint function Φ_1 (15) vanishes identically

$$\frac{1}{2} \int_0^1 \dot{\mathbf{q}}(t)^T \mathbf{G} \dot{\mathbf{q}}(t) dt \rightarrow \min_{\mathbf{q}(t), \Phi_1(\mathbf{f}(\mathbf{q}(t)))=0} \quad (\text{B1})$$

with the constant metric matrix \mathbf{G} (24). The governing equations of the geodesic may be considered as a constrained mechanical system, see Equation (6). Then, the geodesic equation is derived by solving Lagrange's equations of the first kind.⁸⁹ To shorten the expressions, we will suppress the dependence on the time of the coordinate vector. For a constrained mechanical system with n holonomic constraints, the equations read

$$\frac{d}{dt} \frac{\partial L(\mathbf{q}, \dot{\mathbf{q}}, t)}{\partial \dot{\mathbf{q}}} - \frac{\partial L(\mathbf{q}, \dot{\mathbf{q}}, t)}{\partial \mathbf{q}} + \mathbf{R}(\mathbf{q}, \lambda) = \mathbf{0}, \quad (\text{B2})$$

where $\lambda \equiv \lambda(t)$ refers to the vector of the Lagrangian multipliers and $\mathbf{R}(\mathbf{q}, \lambda)$ corresponds to the constraint forces

$$\mathbf{R}(\mathbf{q}, \lambda) \equiv \left(\frac{\partial \Phi_1(\mathbf{f}(\mathbf{q}))}{\partial \mathbf{q}} \right)^T \lambda \equiv \mathbf{J}(\mathbf{q})^T \lambda. \quad (\text{B3})$$

For the considered polygonal chain, the transposed Jacobian of the constraint vector $\mathbf{J}(\mathbf{q})^T$ in Equation (B3) may be computed explicitly as

$$\mathbf{J}(\mathbf{q}(t))^T = \begin{bmatrix} \mathbf{0}_{3 \times 1} & \mathbf{0}_{3 \times 1} & \cdots & \mathbf{0}_{3 \times 1} \\ \mathbf{p}^1(t) & \mathbf{0}_{3 \times 1} & \cdots & \mathbf{0}_{3 \times 1} \\ \mathbf{0}_{3 \times 1} & \mathbf{p}^2(t) & \cdots & \mathbf{0}_{3 \times 1} \\ \vdots & \vdots & \ddots & \vdots \\ \mathbf{0}_{3 \times 1} & \mathbf{0} & \cdots & \mathbf{p}^n(t) \end{bmatrix}. \quad (\text{B4})$$

As we consider no potential function, the Lagrangian function L in Equation (B2) equals the kinetic energy and depends only on the first time derivative of the coordinate vector. Hence, Lagrange's equations of the first kind shorten to

$$\frac{d}{dt} \frac{\partial E(\dot{\mathbf{q}})}{\partial \dot{\mathbf{q}}} + \mathbf{J}(\mathbf{q})^T \lambda = \mathbf{0}, \quad (\text{B5})$$

where the first term of Equation (B5) computes as

$$\frac{d}{dt} \frac{\partial E(\dot{\mathbf{q}})}{\partial \dot{\mathbf{q}}} \equiv \frac{d}{dt} \frac{1}{2} \frac{\partial \dot{\mathbf{q}}^T \mathbf{G} \dot{\mathbf{q}}}{\partial \dot{\mathbf{q}}} = \mathbf{G} \ddot{\mathbf{q}}. \quad (\text{B6})$$

Accounting for the geometric constraints (15) in Equation (B5) explicitly leads us to the differential algebraic equations for the geodesics of the manifold \mathcal{R} in Equation (27)

$$\begin{aligned} \mathbf{G} \ddot{\mathbf{q}} + \mathbf{J}(\mathbf{q})^T \lambda &= \mathbf{0}, \\ \Phi_1(\mathbf{f}(\mathbf{q})) &= \mathbf{0}. \end{aligned} \quad (\text{B7})$$